

ORIENTATION DEPENDENCE OF DISLOCATION STRUCTURE EVOLUTION OF  
ALUMINUM ALLOYS IN 2-D AND 3-D

By

COLIN CLARKE MERRIMAN

A thesis submitted in partial fulfillment  
of the requirements for the degree of:

MASTER OF SCIENCE IN MATERIALS SCIENCE AND ENGINEERING

WASHINGTON STATE UNIVERSITY  
School of Mechanical and Materials Engineering

AUGUST 2007

To the Faculty of Washington State University:

The members of the Committee appointed to examine the thesis of  
COLIN CLARKE MERRIMAN find it satisfactory and recommend that it be accepted.

---

Chair

---

---

---

---

## ACKNOWLEDGEMENTS

I would like to express my deepest respect and gratitude to my advisor Dr. David P. Field for providing me the expert guidance, insight, vision, patience and tremendous help with the presented research. A special thanks Dr. Pankaj Trivedi and Scott Lindeman for their guidance, input, and assistance, without it I would have been lost while programming. I would also like to thank Dr. Hasso Weiland, Randy Burgess, and Julie Smith who are recognized for providing assistance in several areas. Lastly, Dr. Sergey Medyanik and Dr. David Bahr for their time and service as my master's committee members.

My deepest gratitude is offered to Northrop Grumman and Alcoa Technical Center for their support of this research.

ORIENTATION DEPENDENCE OF DISLOCATION STRUCTURE EVOLUTION OF  
ALUMINUM ALLOYS IN 2-D AND 3-D

ABSTRACT

by Colin Clarke Merriman, M. S.  
Washington State University  
August 2007

Chair: David Field

A proper understanding of the relationships that connect deformation, microstructural evolution and dislocation structure evolution is required to extend service lifetime of components, reduce the manufacturing costs, and improve product quality. This requires significant efforts in performing accurate analysis of undeformed and deformed microstructure and identifying the microstructural response to an applied stress, be it in compression tension, or fatigue. Current models are based on observed phenomenology of the process and therefore fail to predict microstructural response of a material beyond a given set of known parameters. Current research is aimed towards making contribution in the areas of (i) microstructural characterization, (ii) understanding the influence of various microstructural parameters on the evolution of dislocation structures and (iii) on relating the physically measurable microstructural parameters to stress response.

In a continuing effort to improve characterization of the dislocation structures of materials the local orientation gradient in deformed polycrystalline samples is examined by the collection of electron back-scatter patterns. Along with the lower bound calculation of the excess dislocation content (planar dataset), a 3-D excess dislocation density calculation is introduced, for serial section datasets, to better understand the bulk microstructural response. In addition, the

excess dislocation density dependence on step size is examined to determine if there is proper step size to be used for the excess dislocation density calculation.

Microstructural evolution during small and large strain channel die deformation of aluminum alloy (AA) 1050 and AA 7050 T7541 was investigated using SEM techniques. From this the orientation dependence of dislocation structures was examined through the initial texture of the material and the plotting of excess dislocation content and Taylor factor in orientation space. It was observed that the Taylor factor and the initial texture has an influence on the deformation behavior and dislocation evolution of aluminum. Neighboring grains (including lattice orientation and dislocation content) and precipitate morphologies also were observed to play a significant role in the microstructural and dislocation response. The observed difference in the evolution of dislocation structures of AA 1050 and AA 7050 T7541 were attributed to their varying manufacturing parameters and differing alloy content.

## TABLE OF CONTENTS

	Page
ACKNOWLEDGEMENTS -----	iii
ABSTRACT -----	iv
LIST OF TABLES -----	ix
LIST OF FIGURES -----	x
<b>CHAPTERS</b>	
<b>1. INTRODUCTION</b> -----	<b>1</b>
1.1 Effects of Microstructure -----	2
1.1.1 Grain Size Effect -----	3
1.1.2 Solid Solution Strengthening -----	4
1.1.3 Strain Hardening -----	4
1.1.4 Precipitation Hardening -----	5
1.2 Crystalline Defects -----	6
1.2.1 Dislocations -----	7
1.3 Observations of Dislocations -----	9
1.4 Outline of the Current Research -----	11
1.5 References -----	13
<b>2. EXCESS DISLOCATION DENSITY CALCULATIONS FROM LATTICE CURVATURE: A COMPARISON OF 2-D AND 3-D DENSITIES</b> -----	<b>14</b>

2.1 Introduction:-----	14
2.1.2 Excess Dislocation Density: -----	16
2.2 Experimental Procedures: -----	21
2.3 Results:-----	24
2.4 Discussion: -----	35
2.5 Conclusions:-----	36
2.6 References: -----	37
<b>3. ORIENTATION DEPENDENCE OF DISLOCATION STRUCTURE EVOLUTION DURING COLD ROLLING OF ALUMINUM-----</b>	<b>38</b>
3.1 Abstract: -----	38
3.2 Introduction:-----	38
3.3 Experimental Details: -----	40
3.4 Results -----	42
3.5 Discussion: -----	50
3.6 Conclusions:-----	52
3.7 References: -----	54
<b>4. ORIENTATION DEPENDENCE OF DISLOCATION STRUCTURE EVOLUTION OF AA7050 -----</b>	<b>56</b>
4.1 Abstract: -----	56
4.2 Introduction:-----	56

4.3 Experimental Details: -----	58
4.4 Results -----	60
4.5 Discussion: -----	69
4.6 Conclusions:-----	71
4.7 References: -----	73
<b>5. CONCLUSIONS</b> -----	<b>75</b>
<b>6. SUGGESTIONS FOR FUTURE WORK</b> -----	<b>78</b>
<b>APPENDIX</b> -----	<b>79</b>
A. 3-D EXCESS DISLOCATION DENSITY CALCULATION C++ CODE -----	79



## LIST OF TABLES

	Page
<b>Table 1.1:</b> Slip systems for FCC Crystals [13]. -----	10
<b>Table 2.1:</b> Excess dislocation density data for Figure 2.5 and 2.6. -----	27
<b>Table 2.2:</b> Excess dislocation density data for Figure 2.9 and 2.10. -----	30
<b>Table 2.3:</b> Excess dislocation density for AA 7050 sample and Cu single crystal dependence of step size ( $\mu\text{m}$ ). -----	34
<b>Table 3.1:</b> Excess dislocation density evolution data for AA 1050 in channel die deformation from undeformed state through 30% deformation for sample 1 and sample 3 by orientation. Dislocation cell size evolution from undeformed through 30% deformation. -----	47
<b>Table 4.1:</b> Excess dislocation density evolution data for AA 7050 T7451 in channel die deformation from undeformed state through 15% deformation by orientation. Dislocation cell size evolution from undeformed through 15% deformation. -----	66

## LIST OF FIGURES

	Page
<p><b>Figure 1.1:</b> Stereographic unit triangle showing five different types of dislocation boundaries (labeled A – E) formed in tensile deformed polycrystalline aluminum [4].-----</p>	3
<p><b>Figure 1.2:</b> Schematic showing the influence of cold work on strength and ductility of material [9]. -----</p>	5
<p><b>Figure 1.3:</b> Schematic showing progressive movement of a dislocation through a 2-D crystal lattice [13].-----</p>	7
<p><b>Figure 1.4:</b> Schematics showing (a) edge dislocation and (b) screw dislocation in simple cubic lattice [13].-----</p>	9
<p><b>Figure 2.1:</b> Diffraction from lattice planes, indicating the geometry that leads to the derivation of Bragg’s law. -----</p>	14
<p><b>Figure 2.2:</b> Schematic showing the formation of Kikuchi pattern using EBSD in SEM [1].-----</p>	16
<p><b>Figure 2.3:</b> Graphical representation of calculation of excess dislocation density. The 2-D calculation assumes lattice curvature in 3<sup>rd</sup> dimension is zero and only accounts for the curvature to the right and below the current. The 3-D calculation takes into account all points surrounding the current point. -----</p>	21
<p><b>Figure 2.4:</b> Channel die deformation setup showing pseudo-internal surface (polished surface).-- -----</p>	22
<p><b>Figure 2.5:</b> ODF of AA 7050 T7 showing a cube texture along with a strong orientation at <math>\{110\}\langle 221\rangle</math>.-----</p>	24

**Figure 2.6:** Serial section 2 (left) and 3 (right) for AA 7050 T7541 (Sample 1) deformed in channel die compression to a 5% height reduction at a strain rate of  $\sim 5.5 \times 10^{-3} \text{ s}^{-1}$ . The 3-D average excess dislocation density was  $1786 \times 10^{12} \text{ m}^{-2}$  and the 2-D density was  $946 \times 10^{12} \text{ m}^{-2}$ .-----25

**Figure 2.7:** 2-D excess dislocation density map for serial section 2 (left) and 3 (right) for Sample 1. The average 2-D excess dislocation density was  $958 \times 10^{12} \text{ m}^{-2}$  and  $942 \times 10^{12} \text{ m}^{-2}$  respectively.--26

**Figure 2.8:** 3-D excess dislocation density map for serial section 2 (left) and 3 (right) for Sample 1. The average 3-D excess dislocation density was  $1851 \times 10^{12} \text{ m}^{-2}$  and  $1722 \times 10^{12} \text{ m}^{-2}$  respectively.-----26

**Figure 2.9:** 3-D OIM dataset of AA 7075 T651, 29 serial sections comprise the 14  $\mu\text{m}$  thick dataset.-----28

**Figure 2.10:** Excess dislocation density maps for the 3-D OIM dataset of AA 7075 T651, 29 serial sections comprise the 14  $\mu\text{m}$  thick dataset with and average 3-D excess dislocation density of  $3063 \times 10^{12} \text{ m}^{-2}$  and an average 2-D density of  $1924 \times 10^{12} \text{ m}^{-2}$ . -----29

**Figure 2.11:** Excess dislocation density plotted with slice depth for comparison of 2-D and 3-D.-----29

**Figure 2.12:** Orientation maps of AA 7050 T7541 deformed in channel die compression to a 10% height reduction at a strain rate of  $\sim 5.5 \times 10^{-3} \text{ s}^{-1}$  showing the declining grain definition as step size increases. Maps obtained using 4 step sizes of 2, 10, 20 and 40  $\mu\text{m}$  with an excess dislocation density of  $174 \times 10^{12} \text{ m}^{-2}$ ,  $32.59 \times 10^{12} \text{ m}^{-2}$ ,  $20 \times 10^{12} \text{ m}^{-2}$ , and  $10 \times 10^{12} \text{ m}^{-2}$ , from left to right.-----31

**Figure 2.13:** Orientation maps showing a variation of the lattice orientation indicating the dislocation structure. Maps obtained using step sizes of 0.2, 5, and 20 with an excess dislocation density of  $1409 \times 10^{12} \text{ m}^{-2}$ ,  $153.59 \times 10^{12} \text{ m}^{-2}$ , and  $33 \times 10^{12} \text{ m}^{-2}$ , from left to right. -----32

**Figure 2.14:** Average excess dislocation density as a function of EBSD step size. The dashed line indicates the expected slope if noise is the only contribution to the measurement. -----33

**Figure 3.1:** ODF of undeformed material showing a weak cube orientation with some retained brass.-----43

**Figure 3.2:** Orientation images, from left to right, of undeformed (a), 5% (b), 10% (c), 15% (d), and 20% (e) reduction. -----44

**Figure 3.3:** Excess dislocation density maps for the orientation images shown in Figure 3.2. Black areas are the lowest density ( $10^{11} \text{ m}^{-2}$ ) areas and regions of low confidence data while the lighter areas are the regions of highest excess dislocation density ( $10^{15} \text{ m}^{-2}$ ). -----45

**Figure 3.4:** Excess dislocation density and dislocation cell size for each deformation step. Excess dislocation density increases with increasing deformation while dislocation cell size decreases.-----  
-----46

**Figure 3.5 and 3.6:** Excess dislocation density by orientation (left), initially the {001} increases at small strains more than the {011} and {111}, by a true strain of 0.025 the {011} and {111} have increased to a greater density than the {001}. Excess dislocation density by orientation (right), {011} and {111} show an increase in excess dislocation density faster than the {001} grains do for true strain steps of 0.05. -----48

**Figure 3.7:** ODF of undeformed material of 2  $\mu\text{m}$  scan shows the texture for a local area only.---  
-----49

**Figure 3.8:** Excess dislocation density plotted in orientation space for 20% deformed material. The  $\{011\}\langle 122\rangle$  orientation shows the strongest dislocation density for the local area. -----50

**Figure 4.1:** ODF of undeformed material contains a combination of cube texture and fcc rolling texture, showing a weak  $\beta$  fiber. Scatter occurs as the  $\beta$  fiber approaches the rotated cube orientation  $\{001\}\langle 110\rangle$  along with the rotated cube orientation while no  $\{111\}\langle uvw\rangle$  component is observed in  $\varphi_2 = 45^\circ$ .-----61

**Figure 4.2:** Orientation images, from left to right, of undeformed (a), 5% (b), 10% (c), and 15% (d) reduction.-----62

**Figure 4.3:** Excess dislocation density maps for the orientation images shown in Figure 2. Black areas are the lowest density ( $10^{11} \text{ m}^{-2}$ ) areas and regions of low confidence data while the lighter areas are the regions of highest excess dislocation density ( $10^{15} \text{ m}^{-2}$ ).-----64

**Figure 4.4:** Excess dislocation density and dislocation cell size for each deformation step. Excess dislocation density increases with increasing deformation while dislocation cell size decreases.-----65

**Figure 4.5:** Excess dislocation density by orientation, initially the  $\{011\}$  start with a very high dislocation density due to the manufacturing process. Both  $\{001\}$  and  $\{111\}$  grains show a fairly linear increase throughout the deformation process, while the  $\{011\}$  jump significantly after 5% deformation.-----67

**Figure 4.6:** Excess dislocation density plotted in ODF space. Initially fairly even distribution with a slight peak at an orientation of  $\{110\}\langle 111\rangle$  in the undeformed state. As deformation increases excess dislocation density increases steadily along the  $\{111\}\langle uvw\rangle$  fiber.-----68

**Figure 4.7:** Taylor factor plotted in orientation space for the undeformed material. A good correlation between regions of high Taylor factor  $>4.0$  and regions of high excess dislocation density exist.-----69

## **Dedication**

This thesis is dedicated to my family

## **CHAPTER – 1**

### **INTRODUCTION**

High performance components in aerospace applications are designed to aid in the reduction of manufacturing costs and extend the service lifetime of the airframe. Commercial, private, and military aerospace programs have driven a need for lighter and tougher materials, which has led to a significant increase in the development and use of advanced structural materials. In addition, the prevalence of computer aided design (CAD) and finite element analysis (FEA) software combined with analytical tools for examining the microstructure and new methods of extrapolating material properties have increased our ability and need to tailor materials to specific applications.

The transportation market has been turning more and more to light weight materials such as aluminum alloys to achieve significant weight-savings and achieve greater fuel economy. Modern military and commercial airframes in active service consist of 80% aluminum by weight. Aluminum is an essential material in manufacturing and is used for its excellent combination of properties, including low density, high-strength, corrosion-resistance, high electrical and thermal conductivity, and fatigue life. The United States aluminum industry is the world's largest, producing about \$39.1 billion in products and exports and processing over 23 billion pounds of metal [1]. Top markets for the aluminum industry are transportation, packaging (i.e. beverage cans), and construction. Aluminum alloys used in structural applications are over-designed to ensure a high factor of safety, which leads to a significant increase in the cost of manufacturing. Typically this is done because of lack of proper understanding of how the initial microstructure



affects the deformation response of the material. Therefore, a proper understanding of the relationships that connect processing conditions, microstructural evolution and mechanical properties is required to optimize the processing parameters, reduce alloy content and improve product quality.

### **1.1 Effects of Microstructure**

During the manufacturing process of aluminum alloys, materials are subjected to a wide range of strain, strain rate and temperature. Since deformation induced during such processing is quite heterogeneous, materials possess a variety of microstructures and properties [2-3]. The initial microstructure of a material plays a critical role in defining the mechanical response of material during deformation and in the evolution of post deformation microstructure. Parameters that influence evolution of microstructure during deformation can be divided into two categories: processing parameters (strain, strain rate, temperature, ect.) and microstructural parameters (dislocation structures, precipitate morphologies, texture, grain size and shape, ect.). The evolution of dislocation boundaries in Al using TEM has shown that there is a strong correlation between evolution of dislocation boundaries and the grain orientation [4]. Figure 1.1 shows that different dislocation structures form in grains with different orientation. The difference between these five regions (marked A – E) lies in the slip systems that are active.

The microstructure and resulting properties of a metal are dynamic in behavior and may be altered by external forces such as applied loads, thermal changes, and chemical environments. Microstructural parameters such as grain size, solid solution morphology, precipitate morphology, dislocation structures etc., can be altered to achieve desired properties. The ability of a metal to plastically deform depends on the ability of dislocations to move, so restricting

dislocation motion makes the material stronger. Below is a brief review on some general strengthening mechanisms achieved by altering microstructure:

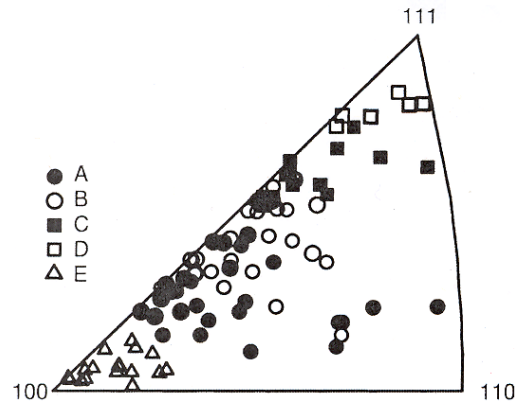


**Figure 1.1:** Stereographic unit triangle showing five different types of dislocation boundaries (labeled A – E) formed in tensile deformed polycrystalline aluminum [4].

### 1.1.1 Grain Size Effect

The yield strength of most crystalline solids increases with decreasing grain size. Quantitatively it is described by the Hall-Petch equation:

$$\sigma_y = \sigma_0 + kD^{-1/2} \dots\dots\dots (1.2)$$

where  $\sigma_0$  is the yield strength of single crystal,  $k$  is a material constant, and  $D$  is the average grain size of the material [5-6]. For yielding of a material to occur throughout the sample it is necessary for the plastic strain to propagate from one grain to next. This means that the stress concentrations that build up at the ends of the first slip band must be sufficient to start yielding in the second grain. The intensity of the stress at the tip of the slip band is dependent on the applied stress, resulting in materials with large grain sizes typically having lower yield strengths.

### 1.1.2 Solid Solution Strengthening

The introduction of solute atoms into solid solution in a solvent-atom lattice produces an alloy which is stronger than the pure metal. There are various ways solute atoms interact with dislocations: elastic interaction, modulus interaction, stacking-fault interaction, electrical interaction, short-range order interaction, long-range order interaction. The resistance to dislocation motion that constitutes solid-solution strengthening can come from one or more of these factors. In solid solutions of FCC metals the hardening is often linearly proportional to the concentration of solute atoms at low concentrations [7].

### 1.1.3 Strain Hardening

Strain hardening is an important industrial process that is used to harden metals by increasing the dislocation density. A high rate of strain hardening implies mutual obstruction of dislocations gliding on intersecting systems. This can come through the interaction of stress fields of the dislocation, the interactions which produce sessile locks, and through the interpenetration of one slip system by another which results in the formation of dislocation jogs. The strength contribution of dislocation structures to the macroscopic flow stress is often represented by an Orowan type equation [8]:

$$\sigma = \sigma_0 + \alpha Gb\rho^{1/2} \dots\dots\dots (1.3)$$

where,  $\sigma$  is the macroscopic flow stress,  $\sigma_0$  is the friction stress,  $\alpha$  is a constant,  $G$  is the shear modulus,  $b$  is the Burger's vector and  $\rho$  is the dislocation density. Figure 1.2 is the schematic showing the influence of cold working on yield stress and ductility of material. It can be seen that with increase in amount of cold work yield stress increases but ductility decreases.

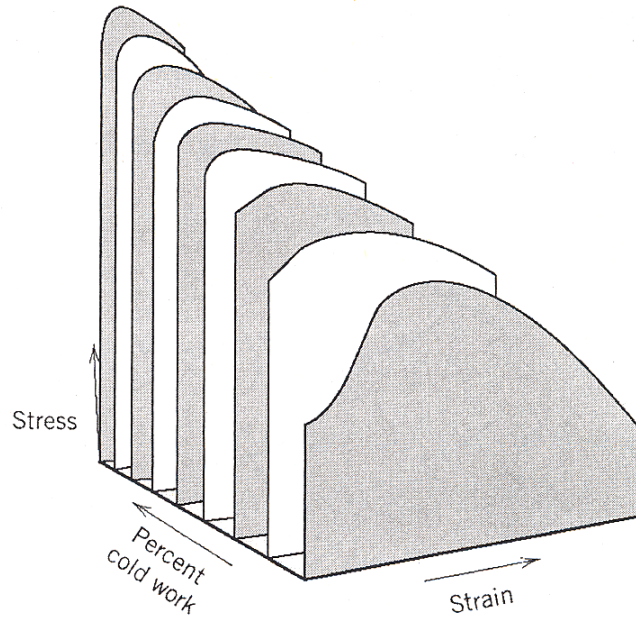


**Figure 1.2:** Schematic showing the influence of cold work on strength and ductility of material [9].

#### *1.1.4 Precipitation Hardening*

Precipitation hardening or age hardening is produced by solution treating, quenching, and aging an alloy. The second phase precipitate remains in solid solution at elevated temperature but precipitates upon aging at a lower temperature. There are several ways in which fine particles can act as barrier to dislocations. They can act as impenetrable particles through which the dislocations can move only by sharp changes in curvature of the dislocation line. Alternatively they can act as coherent particles through which a dislocation can pass, but only at stress levels greater than those required to move dislocations through the matrix phase. The degree of strengthening from second phase particles depends on the morphology of particles in the matrix such as size distribution, inter-particle spacing, size and shape of particles and volume fraction.

## 1.2 Crystalline Defects

Crystalline materials exhibit long-range order in the position and stacking sequence of atoms. Crystalline structures consist of a three dimensional arrangement of lattice points in space, where each lattice point has identical surroundings. Associated with each lattice points is a single atom or group of atoms, depending on the solid under consideration. When a crystal deviates from perfect periodicity with regard to its atomic configuration, it is termed as a defect or imperfection. These defects can be classified into the following groups:

- **Point Defects (Zero Dimensional):** Localized disruptions of the lattice only one or several atoms are called point defects. This includes impurity atoms (substitutional or interstitial) or the absence of an atom (vacancy).
- **Line Defects (One Dimensional):** Line defects are defective regions of the crystal that extend through the crystal along a line. The most important line defect is the dislocation. The dislocation is the defect responsible for the phenomena of slip, by which most metals plastically deform.
- **Planar Defects (Two Dimensional):** Planar defects occupy higher spatial volume than point or line defects. These include grain boundaries, interfaces, stacking faults and twin boundaries.
- **Bulk Defects (Three Dimensional):** Such volume defects are formed by concentration of point or line defects and occupy a spatial volume in 3 dimensions. These include precipitates, voids and cracks and usually occur during processing of materials.

### 1.2.1 Dislocations

The concept of a dislocation was first introduced independently by Orowan [10], Polanyi [11] and Taylor [12] to explain the discrepancy between the observed and theoretical shear strength of metals. They showed that the motion of dislocations through a crystal lattice requires less stress than the theoretical stress and the movement of the dislocations produces a step at the free surface. Figure 1.3 is the schematic of the movement of a dislocation through a lattice such that one atomic bond is broken at a time [13].

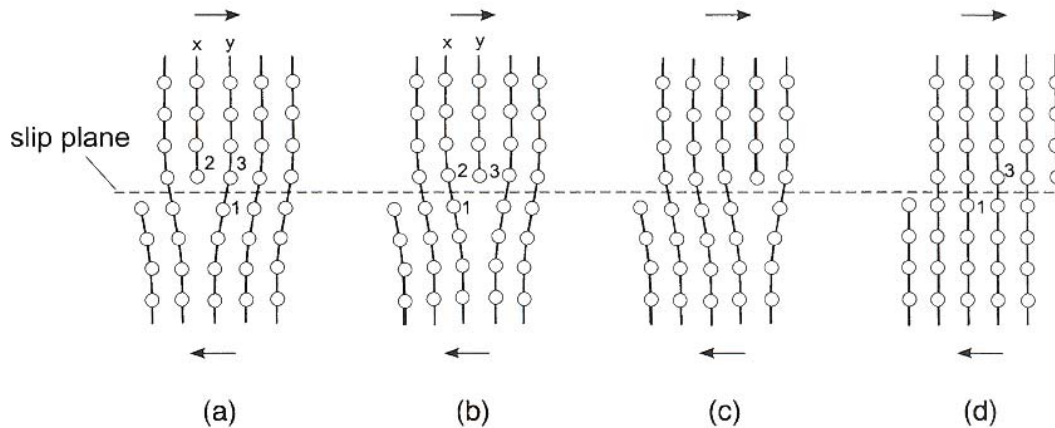


**Figure 1.3:** Schematic showing progressive movement of a dislocation through a 2-D crystal lattice [13].

A dislocation is characterized by its Burger's vector ( $\mathbf{b}$ ), which is a scalar magnitude. The Burger's vector is typically equal to the interatomic vector in the glide plane, or at least a small lattice vector. Dislocations of this type are called perfect dislocations. In certain cases, it is also possible to have a Burger's vector equal to a fraction of a repeat lattice vector. The dislocation is then an imperfect or partial dislocation, and the original lattice structure is not preserved when

the dislocation line is crossed. For example in FCC metals, perfect dislocations of type  $a/2\langle 110 \rangle$  can decompose into two partial dislocations to minimize the energy e.g.  $\frac{a}{2}[10\bar{1}] \rightarrow \frac{a}{6}[2\bar{1}\bar{1}] + \frac{a}{6}[11\bar{2}]$ . The two basic types of dislocations are edge dislocations and screw dislocations. Figure 1.4 shows a visual representation of an edge dislocation (left) and a screw dislocation (right). The shear displacements associated with plastic deformation occur primarily by the movement of dislocations. Planes on which dislocations move is called slip plane and the direction is called the slip direction. The slip planes and direction are those of highest atomic density. The only prerequisite for a plane to be a slip plane is that it contains both the Burger's vector and line direction. For edge dislocations, since the Burger's vector is normal to the line vector, there exists a unique slip plane in which they are able to move. For screw dislocations however, there exist multiple feasible slip planes, as the Burger's vector and line direction are parallel to each other.

Plastic deformation in crystalline solids is inhomogeneous and usually occurs by sliding of blocks of the crystal over one another along definite slip planes and in definite slip directions. Every dislocation then produces slip in a specific direction (parallel to the Burger's vector) and moves on a specific slip plane. Each crystal structure thus has a definite set of slip planes and directions (also known as slip systems). Slip planes in FCC metals are  $\{111\}$  and slip directions are  $\langle 110 \rangle$  (shown in Figure 1.5 and Table 1.1) [13]. Macroscopic slip is observed on a given system when the resolved shear stress reaches the critical value for the onset of dislocation motion, i.e., a stress high enough to overcome the lattice resistance to dislocation motion. The critical resolved shear stress is the value of the resolved shear stress that occurs at the onset of

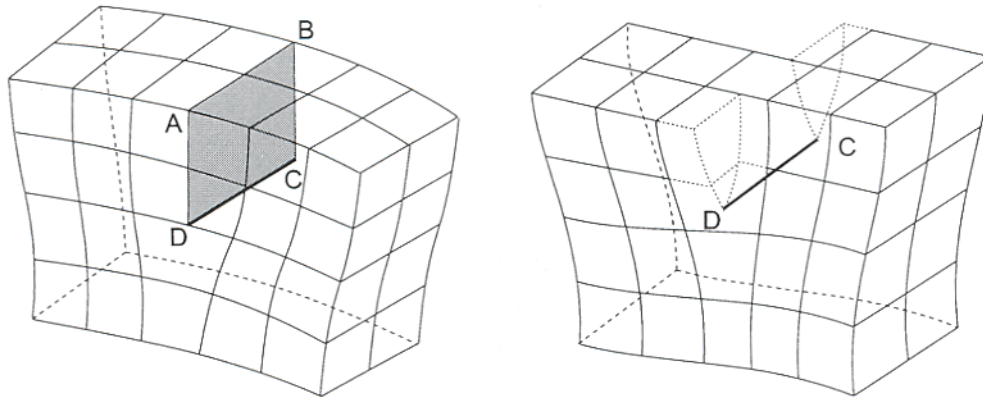


**Figure 1.4:** Schematics showing (a) edge dislocation and (b) screw dislocation in simple cubic lattice [13].

dislocation motion and is the same for all similar slip systems in a crystal. A single crystal subjected to a shear stress can deform extensively with slip on only a single slip system. However in polycrystalline materials, since all grains are oriented differently, each will respond differently when subjected to a shear stress. And if each grain deforms differently, then the region around grain boundaries is subject to complex shape changes if we demand stress and strain continuity to be maintained between grains. According to Taylor, to achieve arbitrary shape change it is necessary to have five independent slip systems operative [14].

### 1.3 Observations of Dislocations

Various techniques have been used over the years to observe dislocations. Almost all experimental techniques for detecting dislocations utilize the strain field around the dislocation to increase its effective size. These techniques can be divided into two categories: those using a chemical reaction with the dislocation and those utilizing a physical change at the dislocation



**Table 1.1:** Slip systems for FCC Crystals [13].

<b>Slip System</b>	<b>Slip Plane</b>	<b>Slip Direction</b>
A2 - Critical system	(1 1 1)	[1 -1 0]
A6 - Critical system	(1 1 1)	[0 1 -1]
A3 - Critical system	(1 1 1)	[1 0 -1]
D1 - Cross-slip system	(-1 1 1)	[1 1 0]
D6 - Cross-slip system	(-1 1 1)	[0 1 -1]
D4 - Cross-slip system	(-1 1 1)	[1 0 1]
B2 - Coplanar system	(1 1 -1)	[1 -1 0]
B5 - Coplanar system	(1 1 -1)	[0 1 1]
B4 - Primary system	(1 1 -1)	[1 0 1]
C1 - Conjugate system	(1 -1 1)	[1 1 0]
C5 - Conjugate system	(1 -1 1)	[0 1 1]
C3 - Conjugate system	(1 -1 1)	[1 0 -1]

site. The chemical methods include etch pit techniques and precipitation techniques. Methods based on the physical structure of the dislocation site include electron microscopy and X-ray diffraction.

Etch pit techniques employ the use of a chemical etchant, which forms a pit around the dislocation sites because of the strain field surrounding the dislocation. Advantages of this technique include its relative ease of use and that it can be applied to bulk samples. However this technique cannot be employed for samples with high dislocation densities and care should be

taken that the pits are formed only at the dislocation sites. Another similar method is to form a visible precipitates along the dislocation line. This technique is called dislocation “decoration” and involves adding a small amount of impurity to form a precipitate after heat treatment. Even though it is possible to see the internal structure of dislocation lines, this technique is not used extensively with metals but is used extensively in semi-conductors.

X-ray microscopy can also be used for detecting dislocations but is not widely used because of low resolution of the techniques, about  $10^5$  dislocations/cm<sup>2</sup>. Transmission electron microscopy (TEM) is the most powerful technique for studying dislocations in solids. Thin samples of  $\sim 1000\text{\AA}$  are electro-polished to make it electron transparent. Individual dislocations can be observed because the intensity of the diffracted beam is altered by the strain field of the dislocation. However, since the information is obtained only from the small volume of sample, this technique does not provide statistically reliable information. Also it is possible to alter the defect structure during sample preparation of the thin films. The technique used in the current investigation provides indirect information about dislocation structure is electron back scatter diffraction (EBSD) and will be discussed further in Chapter 2 [15].

#### **1.4 Outline of the Current Research**

Constitutive models are typically phenomenological in nature, with stress-strain behavior measured and fitted to “state” variables that have little to do with the actual microstructure. By more fully characterizing the microstructure this data can be included and explicitly defined in models. The ultimate goal of this project was to provide experimental data in support of a continuing effort to model excess dislocation density evolution on aluminum alloys. The current

research is focused on development of tools for quantitative understanding of microstructure-property relationship and improved characterization technique that can include sufficient information for models.

Following are the outline and general objectives of the current research:

- Chapter 2 introduces strategies to define and image local orientation gradients in deformed crystalline materials in 2-D and 3-D. Information about the local lattice curvature obtained from EBSD data is used to generate 2-D and 3-D maps showing spatial distribution of scalar parameters that represent local orientation gradient.
- Chapter 3 covers the orientation dependence of dislocation structure evolution during small and large strains at room temperature deformation of AA 1050. A new strategy for plotting the excess dislocation density in orientation space is introduced.
- Chapter 4 covers the orientation dependence of dislocation structure evolution during small and large strains at room temperature deformation of AA 7050. The strategy for plotting the excess dislocation density in orientation space is expanded and compared directly to the Taylor factor, also being plotted in orientation space.
- Chapter 5 summarizes conclusions of the current research.
- Chapter 6 contains suggestions for future work.

## 1.5 References

- [1]. [www.aluminum.org](http://www.aluminum.org) (2007)
- [2]. T.J. Turner, M.P. Miller, N.R. Barton, *Mech. Mat.* 34 (2002) 605-625.
- [3]. O. Engler, M.-Y. Huh, C.N. Tome, *Metal. Mater. Trans.* 31A 9 (2000) 2299-2315.
- [4]. G. Winther, *Mat. Sci. Eng. A309–310* (2001) 486-489.
- [5]. E.O. Hall, *Proc. Phys. Soc. London* 643 (1951) 747.
- [6]. N.J. Petch, *J. Iron. Steel Inst. London* 173 (1953) 25.
- [7]. G.E. Dieter, *Mechanical Metallurgy* (McGraw-Hill 1986, 3<sup>rd</sup> Edition).
- [8]. H. Mecking, U.F. Kocks, *Acta Metall.* 29 (1981) 1865.
- [9]. W.D. Callister Jr., *Materials Science and Engineering: An Introduction* (John Wiley 1999, 5th Edition).
- [10]. E.Z. Orowan, *Z. Phys.* 89 (1934) 605.
- [11]. M.Z. Polanyi, *Z. Phys.*, 89 (1934) 660.
- [12]. G.I. Taylor, *Proc. R. Soc. London* 145A (1934) 362.
- [13]. D. Hull, D.J. Bacon, *Introduction to Dislocations*, (Elsevier, London, UK, 2001).
- [14]. G.I. Taylor, *J. Inst. Met.* 62 (1938) 307.
- [15]. B.L. Adams, S.I. Wright, K. Kunze, *Met. Trans.* 24A (1993) 819.

CHAPTER – 2

**EXCESS DISLOCATION DENSITY CALCULATIONS FROM LATTICE  
CURVATURE: A COMPARISON OF 2-D AND 3-D DENSITIES**

**2.1 Introduction:**

Electron-backscatter diffraction (EBSD) is an SEM-based technique used to obtain local surface information on the crystallographic character of the bulk material. EBSD is a convergent beam technique whereby an electron diffraction pattern is formed by coherently backscattered electrons diffracted by planes matching the Bragg condition,

$$\lambda = 2d \sin \theta \quad \dots\dots\dots (2.1)$$

where  $\lambda$  is the wavelength of the electron beam,  $d$  is the interplanar spacing for a given set of lattice planes and  $\theta$  is the Bragg angle shown in Figure 2.1.

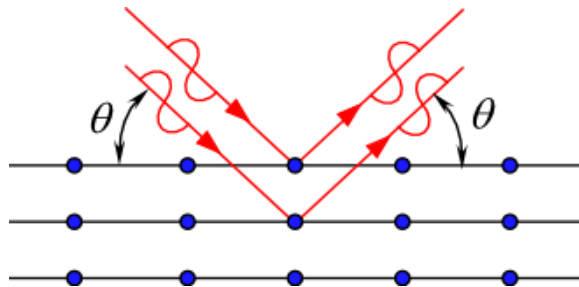


**Figure 2.1:** Diffraction from lattice planes, indicating the geometry that leads to the derivation of Bragg's law.

The collection of an electron backscatter diffraction pattern (EBSP) is carried out by tilting a polished sample to an angle of  $70^\circ$  inside the SEM chamber. When the electrons interact with the sample material, they are inelastically scattered in all directions beneath the surface of the material. As a result there are some electrons that satisfy the Bragg angle for every plane in the crystal. These electrons are elastically scattered as they exit the specimen surface, to form the contrast observed in EBSD patterns. Because the electrons travel from the source in all directions, for each set planes for which the Bragg condition is satisfied, the diffracted beams lie on the surface of a cone whose axis is normal to the diffracted plane. Those cones intersect with a phosphor screen placed in front of the specimen and give rise to the pattern shown in Figure 2.2. Each pair of cones, whose intersection with the phosphor screen produces nearly parallel sets of lines, is termed a Kikuchi band. An image analysis technique, called a Hough transform, is used to detect Kikuchi bands. The Hough transform is given by  $\rho = x \cos \theta + y \sin \theta$ , which integrates intensity along all possible straight lines, reducing all lines in real space to a single point defined by  $(\rho, \theta)$  in Hough space. Usually automated indexing of EBSD patterns is done using sophisticated software algorithms. The whole process from start to finish can take less than 0.005 seconds. One major advantage of the EBSD technique is that measurements can be performed on a large sample area and thus statistically reliable orientation information can be obtained. Resolution of the technique is dependent upon the SEM type and atomic number of the metal. In modern FEG-SEM microscopes an angular resolution is about  $0.5^\circ$  and spatial resolution is 20 nm is possible.

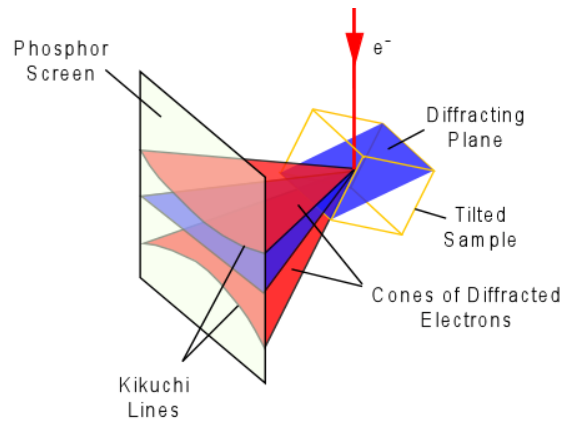


**Figure 2.2:** Schematic showing the formation of Kikuchi pattern using EBSD in SEM [1].

### 2.1.2 Excess Dislocation Density:

During plastic deformation of polycrystalline materials, individual grains do not rotate as a unit but are sometimes subdivided into crystallites rotating independently of one another to accommodate the imposed strain. The reason for grain fragmentation is that the number and selection of simultaneously acting slip systems differs between neighboring volume elements within a grain. This leads to differences in lattice rotations between neighboring elements within a grain when the material is strained. Depending upon the crystal lattice orientation of the grain and its interaction with near neighbors, grains could develop a well defined cell-block structure of similar lattice orientation but rotating at differing rates and sometimes in differing directions. In some instances the lattice rotation rate within a grain changes in a continuous fashion, thus developing long range orientation gradients. Irrespective of the type of grain subdivision, excess dislocations accommodate small lattice rotations. The concept of excess dislocations was first introduced by Nye [2] and further developed by Ashby [3]. During deformation it can be seen that since individual grains do not deform independently of one another, excess dislocations are produced at the grain boundaries to maintain lattice continuity. Nye's tensor,  $\alpha_{ij}$ , is a

representation of a dislocation with Burger's vector  $\mathbf{b}$  and line vector  $\mathbf{t}$ . In Nye's original formulation of the dislocation tensor, dislocation density was described as a number density of lines piercing a plane. The tensor was defined in the following manner:

$$\alpha_{ij} = nb_i t_j \quad \dots\dots\dots (2.2)$$

where  $n$  was the number density of dislocation lines with Burger's vector,  $\mathbf{b}$ , crossing a unit area normal to their unit tangent line vector,  $\mathbf{t}$ . The discretized Burger's vector,  $\mathbf{b}$ , and tangent line vectors,  $\mathbf{t}$ , form  $n$ -pairs of geometric dislocation properties. We can extend Equation 2.2 suggested by Nye, to relate the dislocation density tensor,  $\alpha$ , to the dislocations present in the neighborhood for any crystal structure with the relation,

$$\alpha = \sum_{i=1}^K \rho^i (\mathbf{b}^i \otimes \mathbf{z}^i) \quad \dots\dots\dots (2.3)$$

where, the dislocation dyadic represents a geometrical definition of dislocation  $i$  having Burger's vector  $\mathbf{b}^i$  and slip plane normal direction  $\mathbf{z}^i$ . The sum is over all the dislocations present and  $\rho^i$  is the scalar dislocation density of dislocation  $i$ . Considering continuously-distributed dislocations, Nye's tensor quantifies a special set of dislocations whose geometric properties are not canceled by other dislocations in the crystal. Any dislocation structure that makes no contribution to the dislocation density tensor, such as a dislocation dipole, is termed statistically stored dislocations. Statistically stored dislocations are formed by statistical mutual trapping of dislocations such as dislocation dipoles. A more detailed description of excess and statistically stored dislocations is given by Arsenlis and Parks [4]. Assuming a minimal effect from elastic strain gradients, any crystallite containing non-zero dislocation density tensor components necessarily contains lattice curvature that can be quantified by spatially specific orientation measurements. Such measurements are inherent to automated EBSD scans of crystalline materials. Thus we can relate



the difference in orientation (or misorientation) between two neighboring data points to the Nye dislocation density tensor by the equation:

$$\alpha_{ij} = e_{ikl} g_{jl,k} \dots\dots\dots (2.4)$$

Since the dislocation density tensor has 9 components it is possible, using a linear simplex method, to determine a set of densities of 9 dislocation types which minimizes the total dislocation content. One disadvantage of using this technique is that it does not take into account all the types of dislocations that could contribute to lattice curvature. This limitation could be overcome by using a normal equation lower bound method (as shown by El-Dasher et al. [5]) where Equation 2.3 for FCC materials could be reduced to:

$$\alpha_l = A_{lk} \rho_k \dots\dots\dots (2.5)$$

where,  $k = 1, 18$  and  $l = 1, 9$  and matrix A represents a component of the dislocation dyadic. We can apply  $L^2$  minimization method to Equation 2.5 and compute the densities of all 18 dislocations using the following equation [6]:

$$\rho_{ED} = A^T (AA^T)^{-1} \alpha \dots\dots\dots (2.6)$$

There exist 36 distinct dislocations that can be used to account for slip in face centered cubic crystals, this may be reduced to 18 geometrically distinct dislocations (+b, -b): 6 screw and 12 edge. In the current analysis the assumption that pure edge and pure screw dislocations are only present and the code has been developed to determine the densities of 18 total dislocation types (12 pure edge and 6 pure screw dislocations). Aluminum alloys possess cubic crystal symmetry with any given orientation ‘g’ having 24 geometrically equivalent orientations. Thus to obtain consistent orientation measurements all measured crystal orientations are reduced to

symmetrically equivalent orientations such that the point to point misorientation angle is minimized. Historically the orientation measurements were done on a two dimensional plane of material, resulting in no information about the orientation gradient in the third dimension (z-direction). Thus it was assumed that the orientation gradient in the third dimension was zero, shown in Equation 2.7.

$$\left[ \begin{array}{ccc} \frac{\partial g_{13}}{\partial y} & \frac{\partial g_{23}}{\partial y} & \frac{\partial g_{33}}{\partial y} \\ -\frac{\partial g_{13}}{\partial x} & -\frac{\partial g_{23}}{\partial x} & -\frac{\partial g_{33}}{\partial x} \\ \frac{\partial g_{12}}{\partial x} - \frac{\partial g_{11}}{\partial y} & \frac{\partial g_{22}}{\partial x} - \frac{\partial g_{21}}{\partial y} & \frac{\partial g_{32}}{\partial x} - \frac{\partial g_{31}}{\partial y} \end{array} \right] \dots\dots\dots (2.7)$$

An accurate determination of dislocation density tensor  $\alpha$  requires the information about the orientation gradient in all the three dimensions shown in Equation 2.8 and shown graphically in Figure 2.3.

$$\left[ \begin{array}{cc} \frac{\partial g_{13}}{\partial y} - \frac{\partial g_{12}}{\partial z} & \frac{\partial g_{23}}{\partial y} - \frac{\partial g_{22}}{\partial z} & \frac{\partial g_{33}}{\partial y} - \frac{\partial g_{32}}{\partial z} \\ \frac{\partial g_{11}}{\partial z} - \frac{\partial g_{13}}{\partial x} & \frac{\partial g_{21}}{\partial z} - \frac{\partial g_{23}}{\partial x} & \frac{\partial g_{31}}{\partial z} - \frac{\partial g_{33}}{\partial x} \\ \frac{\partial g_{12}}{\partial x} - \frac{\partial g_{11}}{\partial y} & \frac{\partial g_{22}}{\partial x} - \frac{\partial g_{21}}{\partial y} & \frac{\partial g_{32}}{\partial x} - \frac{\partial g_{31}}{\partial y} \end{array} \right] \dots\dots\dots (2.8)$$

The updated code (Appendix A) has been expanded to include both the 2-D and 3-D dislocation density tensor calculation. In addition, to determine an accurate estimate of excess dislocation density when analyzing polycrystalline materials, it is important to ignore the high angle misorientations (i.e. grain boundaries). The current code, shown in Appendix A, accomplishes this by assigning points with  $>10^\circ$  misorientation an excess dislocation density zero. For data obtained on a single plane, the assumption is made that there is no curvature in the direction normal to the section plane, and the measurement becomes a lower bound of excess dislocation

content to accommodate the observed curvature in the lattice. The inherent uncertainty in orientation determination using automated EBSD techniques is on the order of 0.5 degrees. This measurement “noise” can result in artificially large measured dislocation densities for small distances between neighboring measurement points, since the dislocation density is obtained directly from the curvature tensor equation 2.9,

$$\kappa_{ij} = \frac{\partial \theta_i}{\partial x_j} \dots\dots\dots (2.9)$$

where the denominator is generally the step size of the EBSD scan. To avoid such difficulty, the data must either be filtered through a smoothing algorithm, or the step size should be selected so that the proper measurement is obtained.

The purpose of this chapter is to expand upon the analysis of the local orientation gradient in deformed metals from 2-D planar datasets to 3-D volumetric datasets to determine the density of excess dislocations from lattice curvature measurements. In addition, a determination, in the absence of data smoothing, of what step size should be used to obtain a reasonable estimate of excess dislocation density.

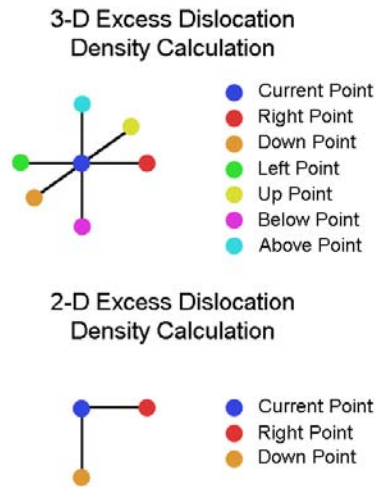


**Figure 2.3:** Graphical representation of calculation of excess dislocation density. The 2-D calculation assumes lattice curvature in 3<sup>rd</sup> dimension is zero and only accounts for the curvature to the right and below the current. The 3-D calculation takes into account all points surrounding the current point.

## 2.2 Experimental Procedures:

One sample of polycrystalline AA 7050 T7451 was deformed and characterized using EBSD. The sample was taken from the quarter plane ( $t/4$  section) of the material and machined to final dimensions of 10 x 20 x 7.5 mm. No further heat treatment was conducted, leaving the material in the as received condition. The sample was deformed at room temperature using channel die compression to a 5% height reduction at a strain rate of  $\sim 5.5 \times 10^{-3} \text{ s}^{-1}$  to simulate cold rolling of aluminum shown in Figure 2.4.

This die imposes a nominally plane strain deformation gradient on the metal similar to that experienced by the aluminum passing through a rolling mill. To avoid problems associated with frictional conditions on the surfaces, the analysis surface is a pseudo-internal interface wherein the specimen is split in two and the mating surfaces are prepared by a fine metallographic polish before deformation [7]. Four serial sections were produced by Hewlett-Packard in Corvallis, Oregon. A second sample dataset was provided by Alcoa Technical Center which consisted of 29 serial section slices of an AA 7075 T651 fatigue specimen. Characterization of the channel die deformed sample was done using a FEI Strata DB 235 with a Schottkey source field-emission gun and Magnum ion column. The data analysis was

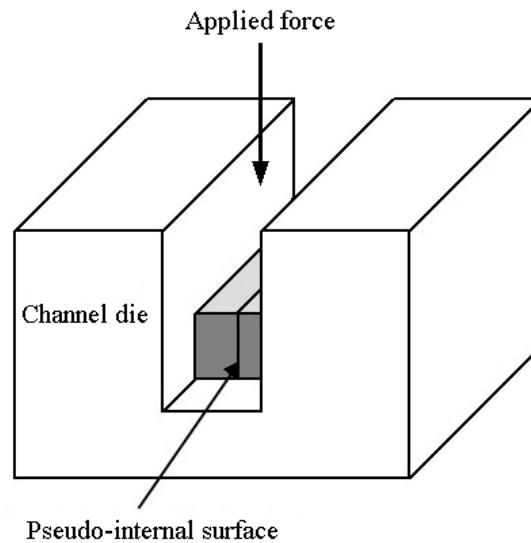


**Figure 2.4:** Channel die deformation setup showing pseudo-internal surface (polished surface).

performed with in house software that had been modified to include the calculation of the dislocation density tensor and the ability to perform this calculation across multiple datasets simultaneously. The 4 dataset serial sections from the channel die deformed AA 7050 (sample 1)

contained ~244,000 points and a volume of  $2500 \mu\text{m}^3$ , the step sized used for these datasets was  $0.25 \mu\text{m}$  with each focused ion beam (FIB) milling process removing  $0.25 \mu\text{m}$  of material. While the 29 dataset serial sections from the fatigue AA 7075 specimen (sample 2) contained 1.45 million points and a volume of  $24824.8 \mu\text{m}^3$ , the step size used for these datasets was  $0.20 \mu\text{m}$  with each FIB milling process removing  $0.50 \mu\text{m}$  of material.

A second sample of AA 7050 T7451 (sample 3) was taken from the quarter plane (t/4 section) of the material and machined to final dimensions of  $10 \times 20 \times 7.5 \text{ mm}$  and was left in the as received condition. The sample was deformed at room temperature using channel die compression to a 10% height reduction at a strain rate of  $\sim 5.5 \times 10^{-3} \text{ s}^{-1}$  to simulate cold rolling of aluminum. The same  $0.40 \text{ mm}^2$  area was scanned using a Schottkey source field-emission scanning electron microscope to collect EBSD patterns at step sizes ranging from  $0.1 \mu\text{m}$  to  $40 \mu\text{m}$ . In addition, a single crystal copper specimen with the  $\langle 2 \ 9 \ 20 \rangle$  direction aligned with the deformation axis, was compressed 10%. EBSD scans were performed using step sizes ranging from  $0.1 \mu\text{m}$  to  $100 \mu\text{m}$  on a polished surface taken from the interior of the specimen. All scans were made near the central part of the prepared surface so as to avoid any edge or surface effects with the compression direction vertical on the images. Data analysis was performed using the aforementioned in house software to calculate the excess dislocation content and determine the effect of step size on the excess dislocation density. The software was set with the following parameters: grain tolerance angle –  $2^\circ$ , minimum grain size – 5 steps.

### 2.3 Results:

Sample 1 and sample 3 arrived in the form of 100 mm thick hot rolled plate. The texture of the AA 7050 samples contains a combination of cube texture and an fcc rolling texture, showing a weak  $\beta$  fiber as shown in the orientation distribution function (ODF) in Figure 2.5. Scatter occurs as the  $\beta$  fiber approaches the rotated cube orientation  $\{001\}\langle 110\rangle$  along with the rotated cube orientation with no  $\{111\}\langle uvw\rangle$  component being observed in  $\varphi_2 = 45^\circ$  [8]. In addition, there is a strong cube orientation component present  $\{001\}\langle 100\rangle$  and brass component  $\{110\}\langle 112\rangle$  as shown in  $\varphi_2 = 0^\circ$ . Figure 2.6 shows the 2<sup>nd</sup> and 3<sup>rd</sup> serial section of sample 1. Figure 2.7 shows the 2-D excess dislocation density maps generated from the same data represented in the orientation images shown in Figure 2.6. Figure 2.8 shows the 3-D

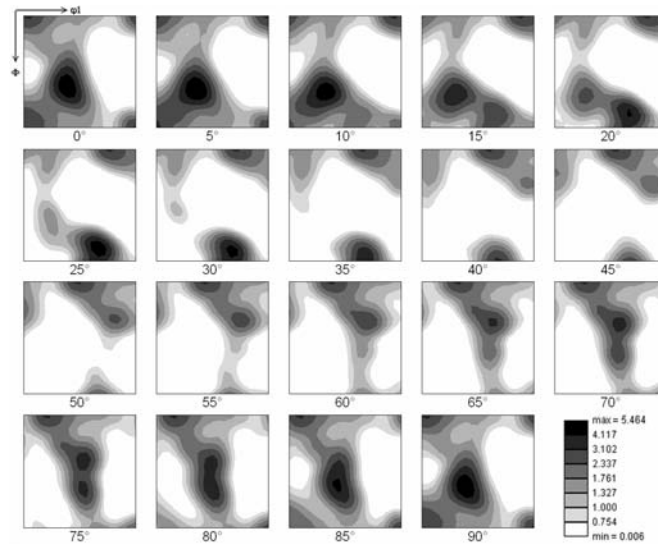


**Figure 2.5:** ODF of AA 7050 T7 showing a cube texture along with a strong orientation at  $\{110\}\langle 221\rangle$ .

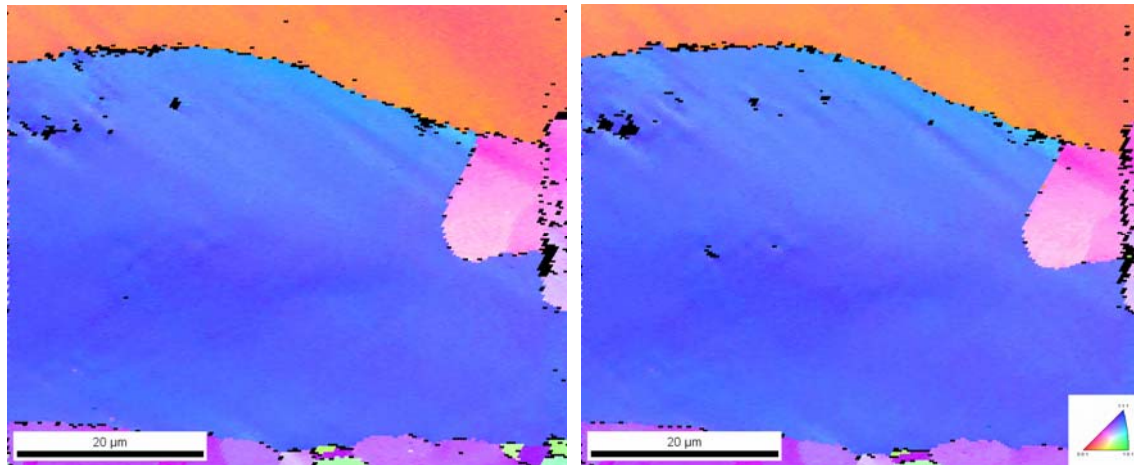


**Figure 2.6:** Serial section 2 (left) and 3 (right) for AA 7050 T7541 (Sample 1) deformed in channel die compression to a 5% height reduction at a strain rate of  $\sim 5.5 \times 10^{-3} \text{ s}^{-1}$ . The 3-D average excess dislocation density was  $1786 \times 10^{12} \text{ m}^{-2}$  and the 2-D density was  $946 \times 10^{12} \text{ m}^{-2}$ .

excess dislocation density maps generated from the same data represented in the orientation images shown in Figure 2.6 in a planar format. White areas are regions of high excess dislocation density while black regions are grain boundaries or data filtered out by the software. The gray scale indicates black for regions of excess dislocation density less than  $10^{11} \text{ m}^{-2}$  to white for densities of  $10^{15} \text{ m}^{-2}$  on a linear scale. Table 2.1 shows all pertinent data calculated for the 2-D and 3-D excess dislocation density. The first and fourth slice of the 3-D dataset are ignored due to there only being one other dataset present for the calculation, resulting in an artificially low density.



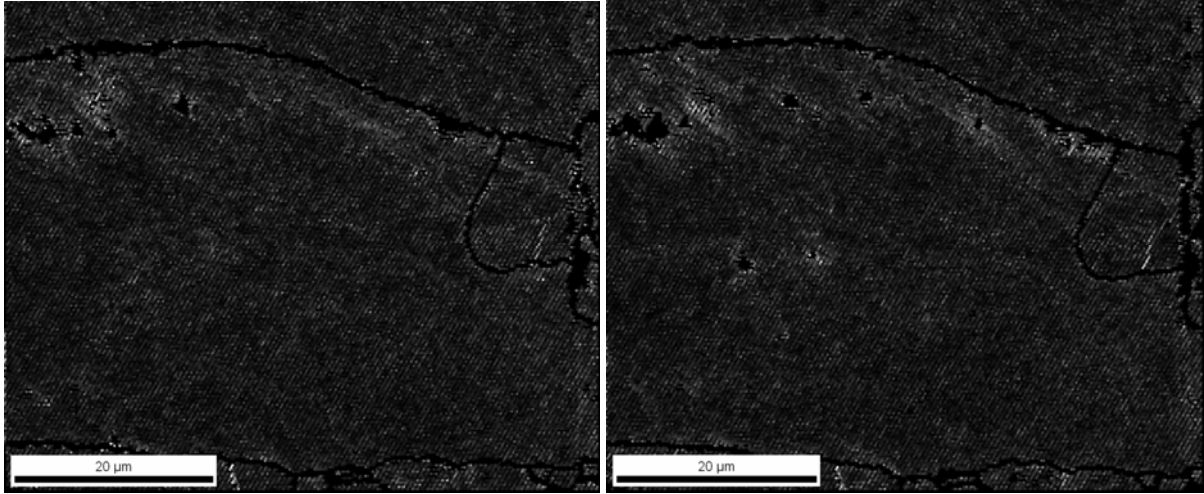


**Figure 2.7:** 2-D excess dislocation density map for serial section 2 (left) and 3 (right) for sample 1. The average 2-D excess dislocation density was  $958 \times 10^{12} \text{ m}^{-2}$  and  $942 \times 10^{12} \text{ m}^{-2}$  respectively.

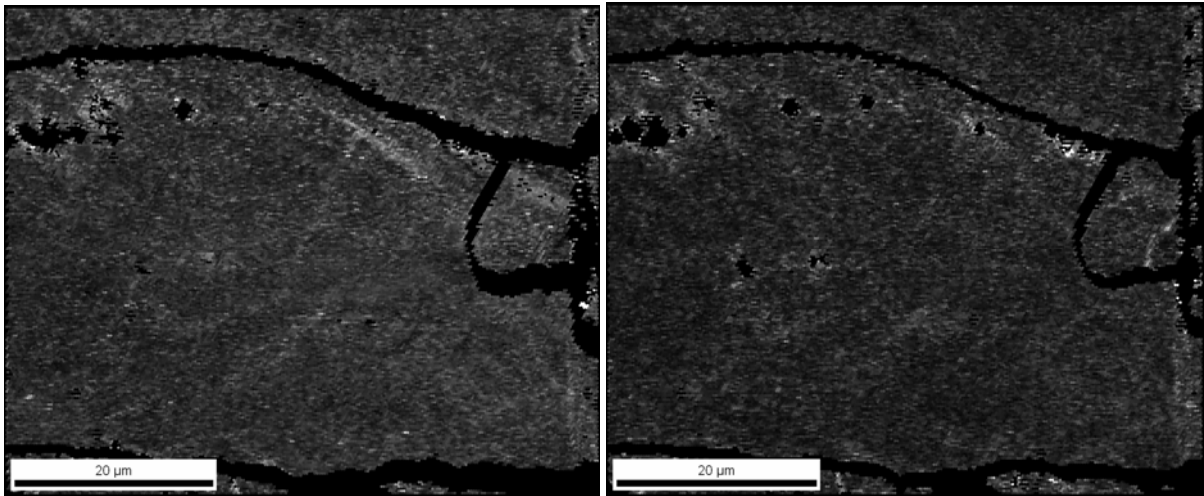


**Figure 2.8:** 3-D excess dislocation density map for serial section 2 (left) and 3 (right) for sample 1. The average 3-D excess dislocation density was  $1851 \times 10^{12} \text{ m}^{-2}$  and  $1722 \times 10^{12} \text{ m}^{-2}$  respectively.

**Table 2.1:** Excess dislocation density data for Figure 2.5 and 2.6.

<b>Table 2.1 – AA 7050 Channel Die Sample</b>		
Serial Section	2-D EDD* ( $10^{12} \text{ m}^{-2}$ )	3-D EDD* ( $10^{12} \text{ m}^{-2}$ )
1	922	--
2	958	1851
3	942	1722
4	965	--
Numerical Average	946	1786

\* - Excess dislocation density

Sample 2 is shown in a 3-D graphical representation in Figure 2.9. Figure 2.10 shows the 3-D graphical representation of the excess dislocation density calculated from the data shown in Figure 2.9. Table 2.2 shows the data for the 29 serial sections in 2- D and 3-D with Figure 2.11 showing that data presented in Table 2.2. White areas are regions of high excess dislocation density while the voids are grain boundaries or data filtered out by the software. The gray scale indicates black for regions of excess dislocation density less than  $10^{11} \text{ m}^{-2}$  to white for densities of  $10^{15} \text{ m}^{-2}$  on a linear scale.

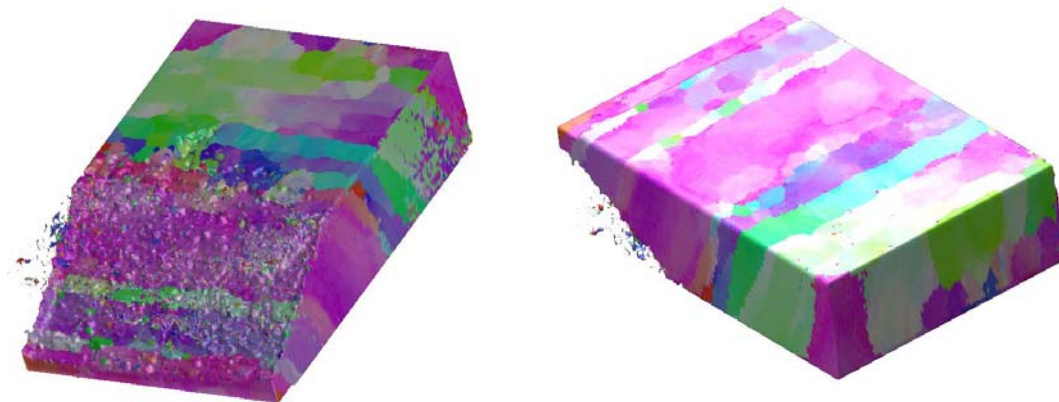


**Figure 2.9:** 3-D OIM dataset of AA 7075 T651, 29 serial sections comprise the 14  $\mu\text{m}$  thick dataset.

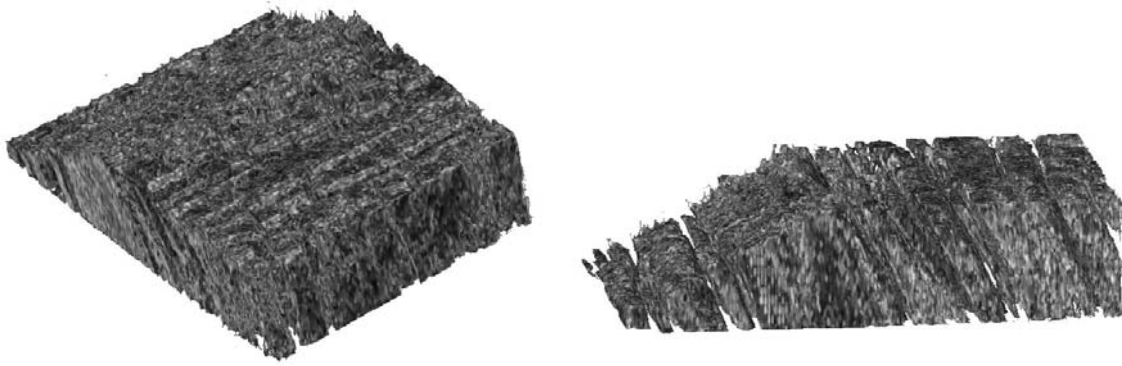


**Figure 2.10:** Excess dislocation density maps for the 3-D OIM dataset of AA 7075 T651, 29 serial sections comprise the 14  $\mu\text{m}$  thick dataset with an average 3-D excess dislocation density of  $3063 \times 10^{12} \text{ m}^{-2}$  and an average 2-D density of  $1924 \times 10^{12} \text{ m}^{-2}$ .

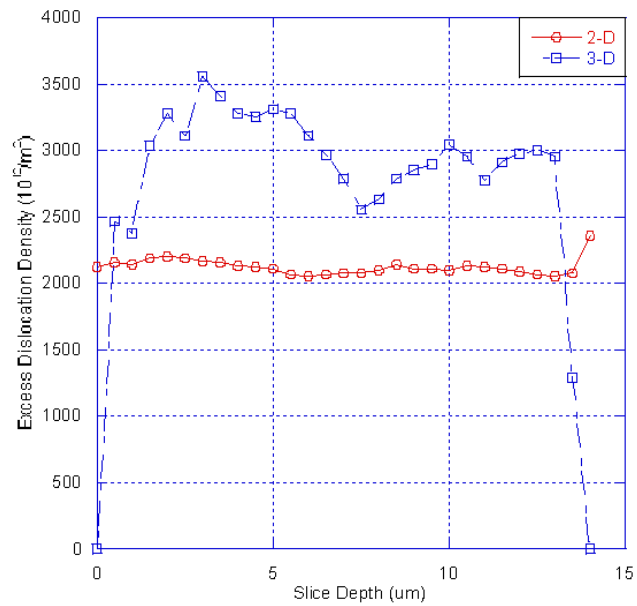


**Figure 2.11:** Excess dislocation density plotted with slice depth for comparison of 2-D and 3-D.

**Table 2.2:** Excess dislocation density data for Figure 2.9 and 2.10.

<b>Table 2.2 – AA 7075 Fatigue Sample</b>			
Serial Section	Scan Depth (μm)	2-D EDD* (10 <sup>12</sup> m <sup>-2</sup> )	3-D EDD* (10 <sup>12</sup> m <sup>-2</sup> )
1	0.0	1921	--
2	0.5	1960	2564
3	1.0	1940	2478
4	1.5	1984	3138
5	2.0	2005	3378
6	2.5	1994	3219
7	3.0	1964	3559
8	3.5	1961	3415
9	4.0	1935	3378
10	4.5	1917	3358
11	5.0	1909	3416
12	5.5	1868	3378
13	6.0	1852	3215
14	6.5	1871	3069
15	7.0	1872	2991
16	7.5	1883	2850
17	8.0	1904	2735
18	8.5	1940	2885
19	9.0	1916	2957
20	9.5	1907	3005
21	10.0	1904	3140
22	10.5	1934	3055
23	11.0	1919	2883
24	11.5	1911	3013
25	12.0	1885	3083
26	12.5	1872	3097
27	13.0	1859	3055
28	13.5	1876	2391
29	14.0	2153	--
Numerical Average		1924	3063
* - Excess dislocation density			

Four chosen scans of sample 3 and the Cu single crystal completed at various step sizes are shown in Figure 2.12 and Figure 2.13 to illustrate decreasing grain definition as step size increases. This has an effect upon the excess dislocation density, as step size increases, excess dislocation density decreases, shown in Figure 2.14 with the corresponding data in Table 2.3 for sample 3 and the copper single crystal. Staker and Holt used TEM imaging techniques to measure the dislocation density in a Cu specimen deformed 10% in tension to be  $118 \times 10^8 \text{ cm}^{-2}$  [9].

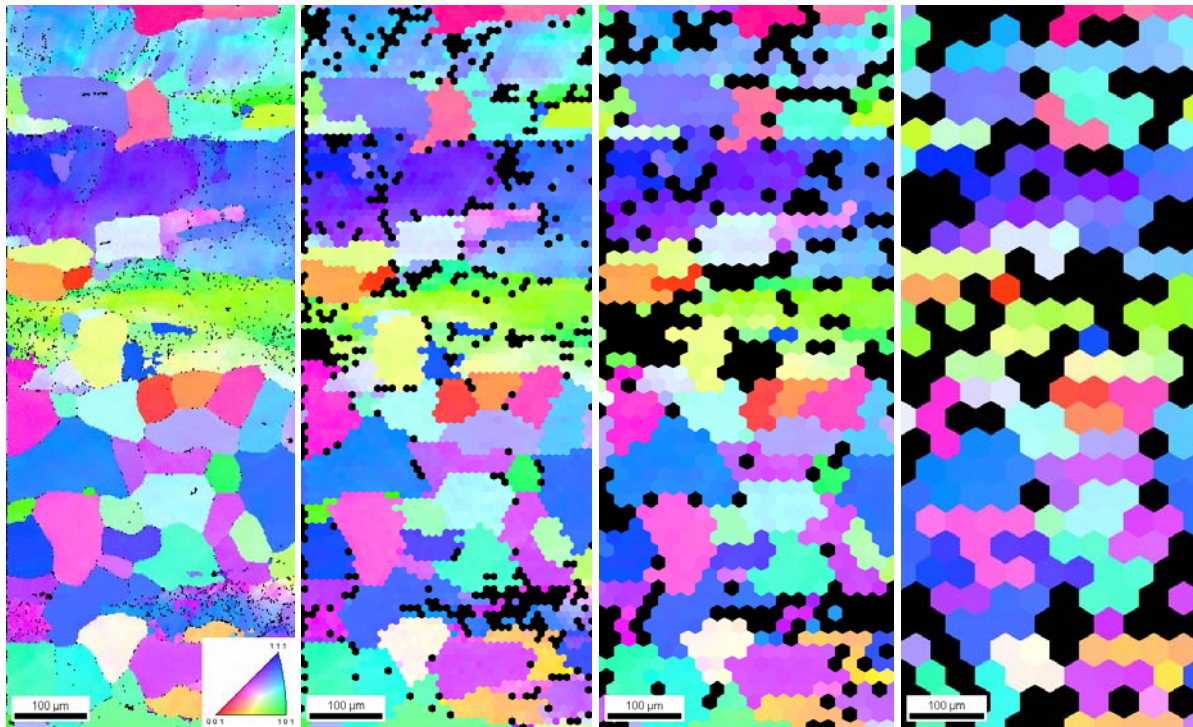


**Figure 2.12:** Orientation maps of AA 7050 T7541 deformed in channel die compression to a 10% height reduction at a strain rate of  $\sim 5.5 \times 10^{-3} \text{ s}^{-1}$  showing the declining grain definition as step size increases. Maps obtained using step sizes of 2, 10, 20 and 40  $\mu\text{m}$  with an excess dislocation density of  $174 \times 10^{12} \text{ m}^{-2}$ ,  $32.59 \times 10^{12} \text{ m}^{-2}$ ,  $20 \times 10^{12} \text{ m}^{-2}$ , and  $10 \times 10^{12} \text{ m}^{-2}$ , from left to right.

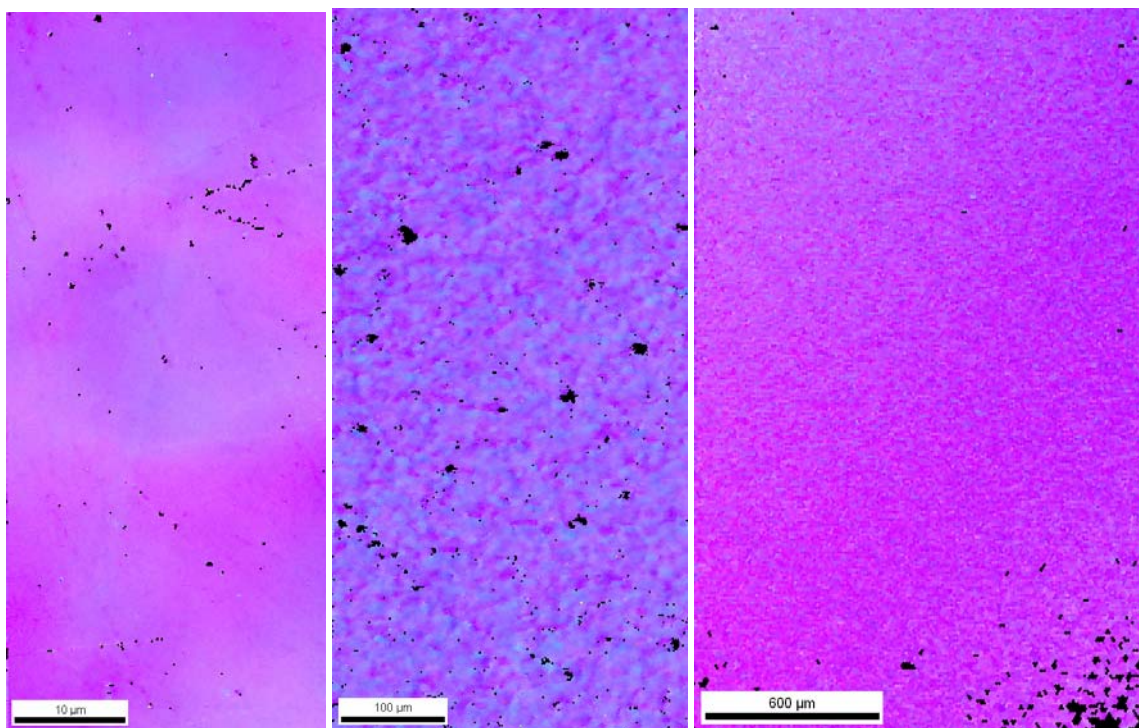


**Figure 2.13:** Orientation maps showing a variation of the lattice orientation indicating the dislocation structure. Maps obtained using can step sizes of 0.2, 5, and 20 with an excess dislocation density of  $1409 \times 10^{12} \text{ m}^{-2}$ ,  $153.59 \times 10^{12} \text{ m}^{-2}$ , and  $33 \times 10^{12} \text{ m}^{-2}$ , from left to right.

Similar results were obtained by Heuser using neutron scattering techniques who measured  $1.9 \times 10^{10} \text{ cm}^{-2}$  at 16% compression of Cu single crystals [10]. A comparison of Figure 2.11 with measured values of the dislocation density as quoted from the literature shows order of magnitude agreement with the EBSD measured densities from step sizes of 10-50  $\mu\text{m}$ .

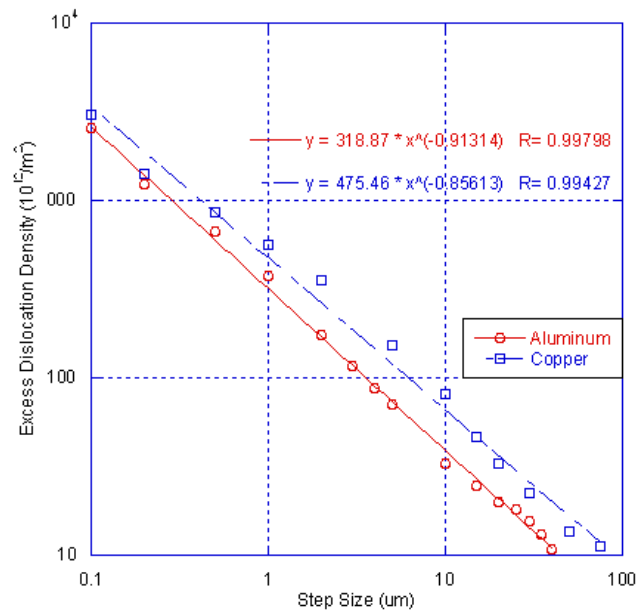


**Figure 2.14:** Average excess dislocation density as a function of EBSD step size. The dashed line indicates the expected slope if noise is the only contribution to the measurement.



**Table 2.3:** Excess dislocation density for AA 7050 sample and Cu single crystal dependence of step size ( $\mu\text{m}$ ).

<b>Table 2.3 – EDD Dependence on Step Size</b>		
Step Size	AA 7050 EDD* ( $10^{12} \text{ m}^{-2}$ )	Copper EDD* ( $10^{12} \text{ m}^{-2}$ )
0.1	2580.8	3049.2
0.2	1226.4	1409.8
0.5	667.43	850.88
1	376.13	559.58
2	174.18	357.63
3	117.01	--
4	87.22	--
5	70.25	153.74
10	32.59	80.84
15	24.68	46.33
20	20.15	33.01
25	18.13	--
30	15.51	22.26
35	13.01	--
40	10.83	--
50	--	13.73
75	--	11.26
* - Excess dislocation density		

## 2.4 Discussion:

For sample 1 the first and fourth serial sections have no excess dislocation density because there is only one neighboring dataset, this results in a value of zero for all orientations. The second and third serial sections show approximately twice the density in 3-D when compared to the 2-D,  $\sim 1786 \times 10^{12} / \text{m}^{-2}$  and  $\sim 950 \times 10^{12} / \text{m}^{-2}$  respectively. The current 3-D code calculates the density by dividing the points into two groups, 1<sup>st</sup> group – right, down, and below points, 2<sup>nd</sup> group – left, up, and above points, and the misorientation is averaged between 1<sup>st</sup> group and 2<sup>nd</sup> group, shown in Equation 2.10.

$$\frac{1}{2} \left( \frac{\partial g_{13}}{\partial y} - \frac{\partial g_{12}}{\partial z} \right) + \frac{1}{2} \left( \frac{\partial g_{13}}{\partial y} - \frac{\partial g_{12}}{\partial z} \right) \dots\dots\dots (2.10)$$

Another point that should be noted when comparing the 3-D and 2-D excess dislocation maps is the grain boundaries for the 3-D maps are much larger. The misorientation filters ( $>10^\circ$ ) were expanded from 2-D to 3-D, resulting in points from above and below the current point to be taken into account examined prior to the calculation. The consequence is more data points are assigned a value of zero.

Sample 2's results agreed with that of sample 1, showing an average 3-D excess dislocation density of  $3063 \times 10^{12} / \text{m}^{-2}$  and average 2-D density of  $1924 \times 10^{12} / \text{m}^{-2}$ . This dataset also proved the validity of the software on datasets with 20+ serial sections and the ability to use existing software to display the data in a graphical form.

In the absence of data smoothing, it seems reasonable to adopt the dislocation cell diameter as the step size of the EBSD scan in order to measure excess dislocation content. This minimizes the contribution of the orientation measurement uncertainty and offers the best chance to obtain reasonable data. A priori knowledge of the character of the dislocation distribution is

required in that a reasonable step size can be estimated from the expected dislocation cell size to obtain a proper measurement of excess dislocation content in deformed crystals. In addition, it was observed in the 3-D datasets that the spacing between the serial sections influences the excess dislocation density in the same manor as varying the step size in 2-D datasets. One would conclude that understanding the bulk character of the material would be crucial to determining an appropriate slice depth for serial sectioning. Assuming that statistically the microstructure is the same in all three dimensions it would be reasonable to apply the same slice depth as step size, however, if a focused ion beam is employed, this would be unreasonable for samples with large dislocation cell diameters but could be accomplished by mechanical polishing.

## **2.5 Conclusions:**

Two samples of Al 7050 were deformed in channel die compression to a 5% height reduction. One sample had four serial sections of EBSD data collected through OIM and FIB milling. An average 3-D excess dislocation density of  $1786 \times 10^{12} \text{ m}^{-2}$  was calculated while the average 2-D density was  $946 \times 10^{12} \text{ m}^{-2}$ . An AA 7075 sample dataset collected from tensile fatigue specimen with 29 serial sections provided by Alcoa Technical Center showed an average 3-D excess dislocation density of  $3063 \times 10^{12} \text{ m}^{-2}$  and an average 2-D density of  $1924 \times 10^{12} \text{ m}^{-2}$ . The second AA 7050 sample and a single crystal copper dataset were used to show the influence of step size of the excess dislocation density. It was observed as the step size was decreased (i.e.  $1 \mu\text{m} \rightarrow 0.2 \mu\text{m}$ ) the excess dislocation density increased following a power law curve. Also for 3-D calculations the spacing between serial sections has the same effect as increasing or decreasing the step size. The same trends were observed in polycrystalline and single crystal datasets.

## 2.6 References:

- [1]. S.I. Wright, *Electron Backscatter Diffraction in Materials Science*, ed. A.J. Schwartz, M. Kumar, and B.L. Adams (Kluwer Academic/Plenum Publishers, New York 2000).
- [2]. J.F. Nye, *Acta Metall.* 1, (1953) 153.
- [3]. M.F. Ashby, *Phil. Mag.* 21, (1970) 399.
- [4]. A. Arsenlis, D.M. Parks, *Acta Mat.* 47, (1999) 1597.
- [5]. B.S. El-Dasher, B.L. Adams, A.D. Rollett, *Scripta Mat.* 48, (2003) 141.
- [6]. G.B. Dantzig, *Linear Programming and Extensions* (Princeton University Press) 1963.
- [7]. S. Panchanadeeswaran, R.D. Doherty, R. Becker, *Acta Mater.* 44 (1996) 1233-1262.
- [8]. O. Engler, M.-Y Huh, C.N. Tome, *Metall. Mater. Trans. A*, 31A (2000) 2299-2315.
- [9]. M.R. Staker, D.L. Holt, *Acta Metall.* 20 (1972) 569.
- [10]. B.J. Heuser, *Appl. Cryst.* 27 (1994) 1020.

## CHAPTER – 3

### **ORIENTATION DEPENDENCE OF DISLOCATION STRUCTURE EVOLUTION DURING COLD ROLLING OF ALUMINUM**

#### **3.1 Abstract:**

A well-organized dislocation structure forms in many polycrystalline metals during plastic deformation. This structure is described qualitatively with no explanation of the quantitative characterization. In this work, the evolution of dislocation structure in commercial purity aluminum is described by means of the excess dislocation density and by quantitative characterization of the cell structure as seen on a plane surface. The measurements were performed on a pseudo-internal surface of a split specimen deformed by channel die deformation. The results show a clear dependence of cell structure formation on orientation of the crystallite with respect to the imposed deformation gradient with the largest excess dislocation density occurring in grains of  $\{011\}[122]$  orientation for plane strain deformation. Neighboring grain and non-local effects are shown to be of importance in the type of dislocation structures that evolve.

#### **3.2 Introduction:**

Evolution of dislocation structures and dislocation-dislocation interactions control the deformation response of polycrystalline materials. As deformation increases in a material, grains

begin to break into volume elements that decrease in size with increasing strain. These volume elements are characterized by two different types of boundaries, incidental dislocation boundaries and geometrically necessary boundaries. Incidental dislocation boundaries (IDB) form by the random trappings of dislocations and geometrically necessary boundaries (GNB) form between regions with one or more different operating slip systems to accommodate the accompanying difference in lattice rotation [1]. These boundaries contain both statistically stored dislocations (redundant, +b -b), which do not contribute significantly to a net lattice rotation, and excess dislocations (non-redundant, often termed geometrically necessary dislocations) that contribute to the net lattice rotation [2-4]. It has been observed by various authors that the character of dislocation structures formed is a function of the lattice orientation with respect to the imposed deformation gradient [5-7]. The presence of these deformation gradients in a material give rise to a lattice rotation  $\theta$  and a net Burger's vector resulting in a rotation. The purpose of the present work is to obtain experimental data of dislocation structure evolution using electron back-scatter diffraction (EBSD), in support of the development of a three dimensional crystal plasticity model to describe the deformation behavior of aluminum alloys. Basic to this model is the concept that the material behavior is controlled by the motion and interaction of excess dislocations. The evolution of dislocation density depends on the divergence of dislocation fluxes associated with the inhomogeneous nature of plasticity in crystals [8-9]. Dislocation structure evolution during cold deformation of fcc polycrystals has been extensively investigated over the past couple of decades with primary emphasis on a qualitative description of the evolving structures and their relation to mechanical properties [10-15]. In the present experiments a channel die is used to simulate cold rolling of aluminum. This die imposes a nominally plane strain deformation gradient on the metal similar to that

experienced by the aluminum passing through a rolling mill. To avoid problems associated with frictional conditions on the surfaces, the surface scanned was a pseudo-internal interface wherein the specimen is split in two and the mating surfaces are prepared by a fine metallographic polish before deformation [16]. This surface is suitable for characterization by electron backscatter diffraction at various steps through the deformation process because it is protected from the majority of the shear deformation characteristic of the specimen surfaces in channel die deformation.

### **3.3 Experimental Details:**

Commercial purity polycrystalline aluminum (Al 1050) was obtained as industrially hot-rolled thick plate (~50 mm thick). Four samples were prepared with dimensions of 30 x 35 x 10 mm<sup>3</sup> and cross rolled at room temperature to a reduction of 40%. The samples were then machined to final dimensions of 11 x 22 x 7.5 mm<sup>3</sup>. They were annealed for 1.5 hours at 450°C to obtain a relatively dislocation free recrystallized structure. Two of the samples were deformed at room temperature by channel die compression in true strain increments of ~0.05 to a 30% height reduction at a strain rate of  $\sim 5.5 \times 10^{-3} \text{ s}^{-1}$ . The other two samples were deformed in true strain increments of ~0.005 to a 5% height reduction at a strain rate of  $\sim 5.5 \times 10^{-3} \text{ s}^{-1}$ . This form of plain strain deformation was used to impose the idealized deformation seen in rolling. TEFLON film was placed between the two samples and the samples and the die walls to prevent galling.

EBSD analysis was performed using a Schottky source field-emission scanning electron microscope. Prior to channel die deformation an 80 mm<sup>2</sup> area was scanned using a 25 μm step size to collect the initial texture. All subsequent scans were of the same 0.85 mm<sup>2</sup> area with a 2 μm step size. The scans were centered in the middle of the sample to exclude edge effects and any anomalous effects created by the punch or the die. The smaller step size was used in this area

to obtain local information about point to point misorientation within grains allowing for calculation of excess dislocation density, dislocation cell size, and local orientation distribution of dislocations. Black regions in orientation images are regions with low confidence index (CI<0.2) data. The black regions in excess dislocation density images are either bad data or regions of low dislocation density. Misorientations of 5° or greater are ignored, so data points along grain boundaries generally have a low apparent dislocation density.

The data analysis was performed with software similar to TSL OIM Analysis 5.1, but that had been modified to include calculation of the dislocation density tensor. The software was set with the following parameters: grain tolerance angle – 2°, minimum grain size – 5 steps. All averages are number averages which translate directly to averages of the grain area owing to the principle of DeLesse and the measurement strategy where data points are taken over a regular hexagonal array. Taylor factors for the given orientations were calculated using the family of active slip systems for FCC metals ( $\{111\}\langle 1-10\rangle$ ) and the plane strain deformation gradient;  $\sigma_{xx}=1$ ,  $\sigma_{zz}=-1$ ,  $\sigma_{yy}=\sigma_{xy}=\sigma_{xz}=\sigma_{yz}=0$ .

The combined expected error of the hardware and software used in these calculations was  $\sim 1.35 \times 10^6 \text{ m}^{-2}$ . This was calculated by taking the uncertainty in the EBSD pattern measurement from point to point (0.5°), assuming that both points are actually of the same orientation. A file with this data was then generated and run through the excess dislocation density function to determine the density. A value was also calculated using the simple relation between lattice curvature and the content of parallel edge dislocations of the same sign ( $\theta = b/D$ , such as for a low angle boundary) assuming the same parameters as the dataset (2  $\mu\text{m}$  step size). The calculated dislocation content for this determination was  $1.23 \times 10^6 \text{ m}^{-2}$  while the software returned a value of  $1.48 \times 10^6 \text{ m}^{-2}$ .



### 3.4 Results

The texture resulting from cross rolling and recrystallization of the Al 1050 samples was a weak cube orientation  $\{001\}\langle 100\rangle$  with some retained brass texture  $\{110\}\langle 112\rangle$  as shown in the constant  $\varphi_2$  cross section crystallite orientation distribution function (ODF) in Figure 3.1. Figure 3.2 shows the progression of orientation images obtained from a given area of one of the samples from the undeformed state to a state of 20% height reduction, the 25% and 30% height reduction maps are not shown because the samples were repolished showing a different region. The undeformed orientation image shows a recrystallized structure with a large variation in grain size most likely a result of the processing of the sample. No lattice curvature is apparent in the undeformed material. The Taylor factor was calculated for  $\{001\}\langle 100\rangle$  orientations to be 2.4 for the given deformation state, while  $\{011\}\langle 01-1\rangle$  and  $\{111\}\langle 01-1\rangle$  grains each had a Taylor

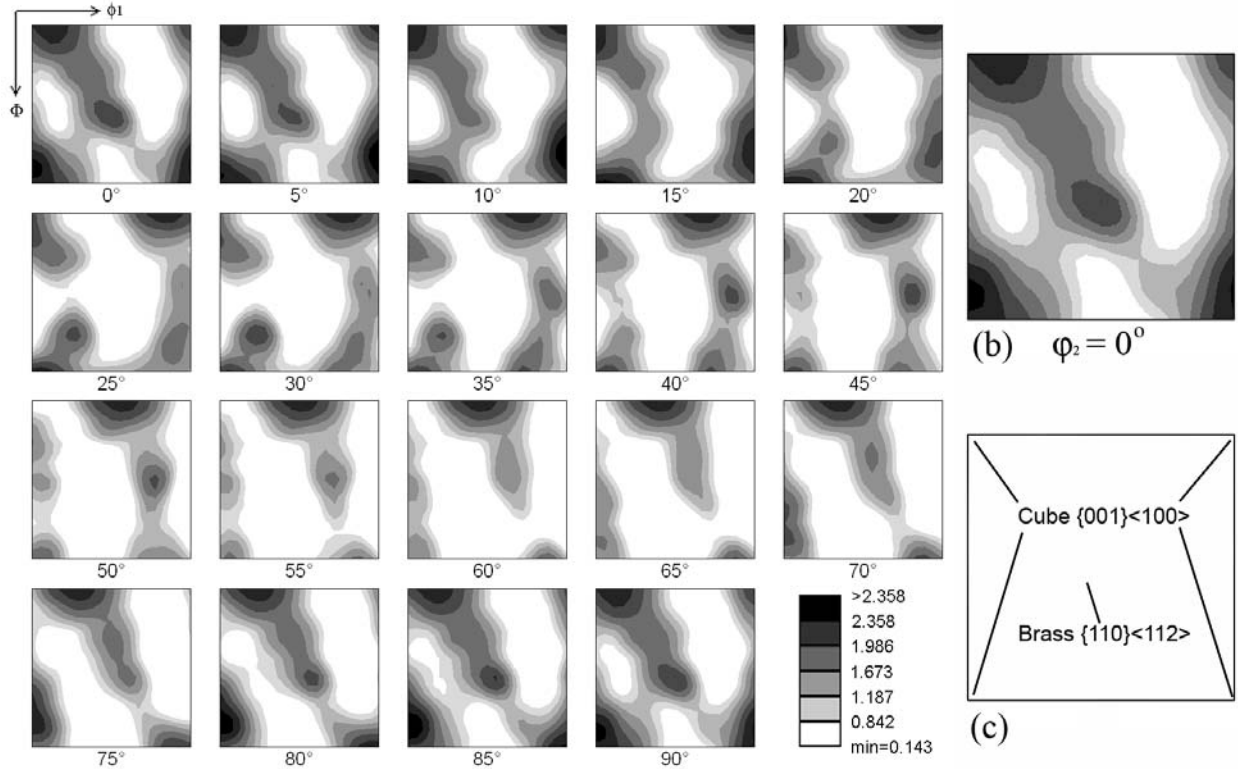


**Figure 3.1:** ODF of undeformed material showing a weak cube orientation with some retained brass.

factor of  $\sim 4.0$ . This would indicate that the  $\{011\}$  and  $\{111\}$  grains should not deform until the  $\{001\}$  grains had hardened sufficiently to initiate slip in the grains of higher Taylor factor. Ultimately the higher Taylor factor grains would have a higher excess dislocation density due to the increased slip necessary for unit strain in these grains. On the other hand the  $\{001\}$  grains should initially deform easily resulting in a higher excess dislocation density but as the samples proceed through large deformation steps the excess dislocation density should not increase as rapidly as the  $\{011\}$  and  $\{111\}$  type grains. This is because the low Taylor factor means that

these grains are “soft” in relation to the neighboring structure and will deform first, resulting in an increased dislocation density. As these harden due to the cold work, the grains with a higher

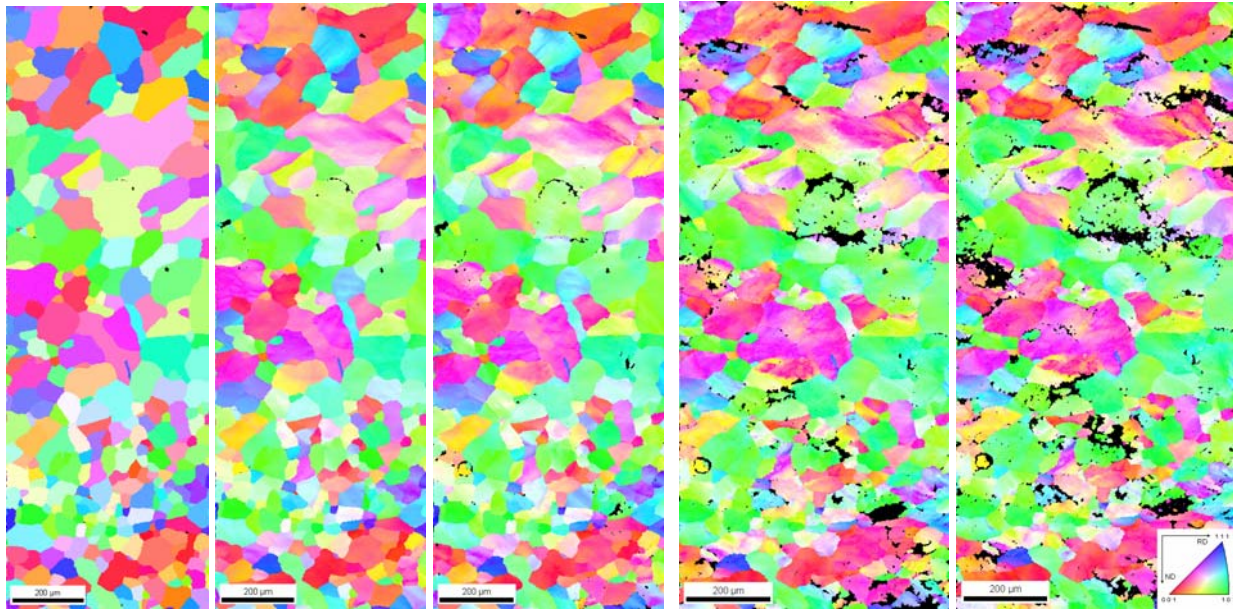


**Figure 3.2:** Orientation images, from left to right, of undeformed (a), 5% (b), 10% (c), 15% (d), and 20% (e) reduction.

Taylor factor will deform. Because of the increased Taylor factor these require more dislocation motion per unit strain to deform, therefore the density will increase at a more rapid rate than in these grains with a lower Taylor factor. This trend was observed experimentally when the excess dislocation density was calculated. Neighboring grains influence this behavior by constraints imposed upon deformation of softer grains by load shielding from grains of higher Taylor factor, resulting in dislocation density evolution to be less predictable for these regions.

Figure 3.3 shows the excess dislocation density maps generated from the same data represented as the orientation images shown in Figure 3.2. White areas are regions of high excess

dislocation density while black regions are grain boundaries or bad data filtered out by the software. The gray scale indicates black for regions of excess dislocation density less than  $10^{11}$   $\text{m}^{-2}$  to white for densities of  $10^{15}$   $\text{m}^{-2}$ . Regions of highest density occur where grain to grain

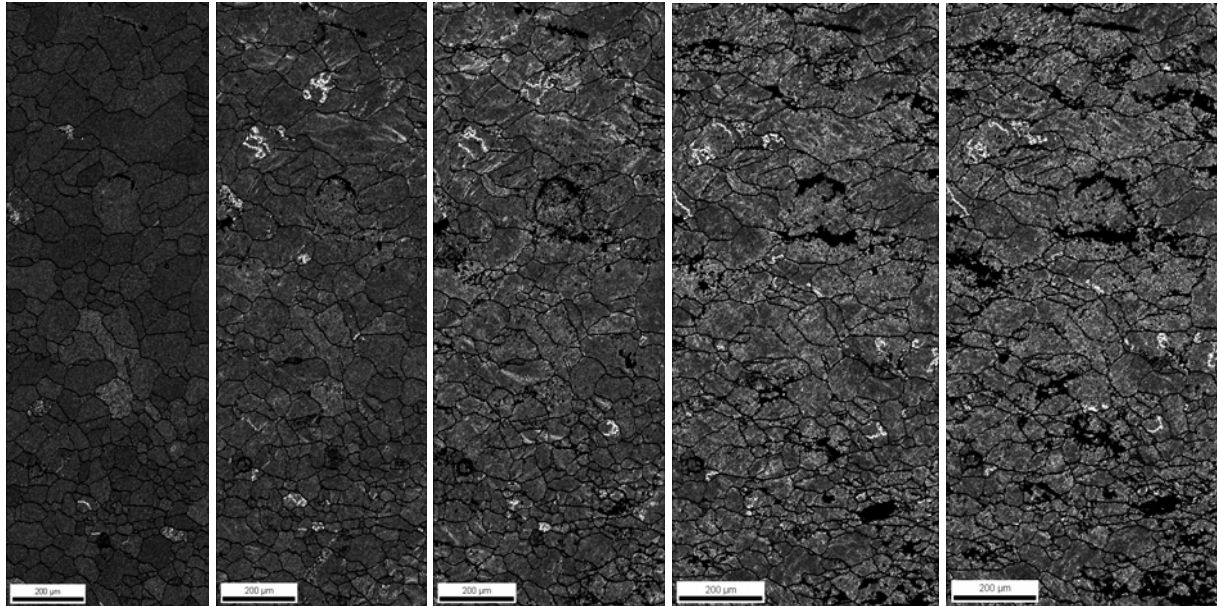


**Figure 3.3:** Excess dislocation density maps for the orientation images shown in Figure 3.2. Black areas are the lowest density ( $10^{11}$   $\text{m}^{-2}$ ) areas and regions of low confidence data while the lighter areas are the regions of highest excess dislocation density ( $10^{15}$   $\text{m}^{-2}$ ).

interaction is the greatest, resulting in hard grains deforming very little while imposing greater deformation on the soft grains. As the excess dislocation density increases there is more dislocation-dislocation interaction, resulting in an increasingly well-defined grain substructure. The undeformed material is free of significant dislocation structure and the dislocation cell size was calculated to be the same as the grain size. Subsequent dislocation cell sizes decreased with each deformation step and the excess dislocation density increased as shown in Figure 3.4 and Table 3.1, which was calculated using in-house software from lattice curvature data, collected

using EBSD. With respect to specific orientations for small deformation steps, incrementally the  $\{001\}$  grains increase the most initially but are over-taken in excess dislocation density around a true strain of 0.025 shown in Figure 3.5. This trend continues through the rest of the deformation

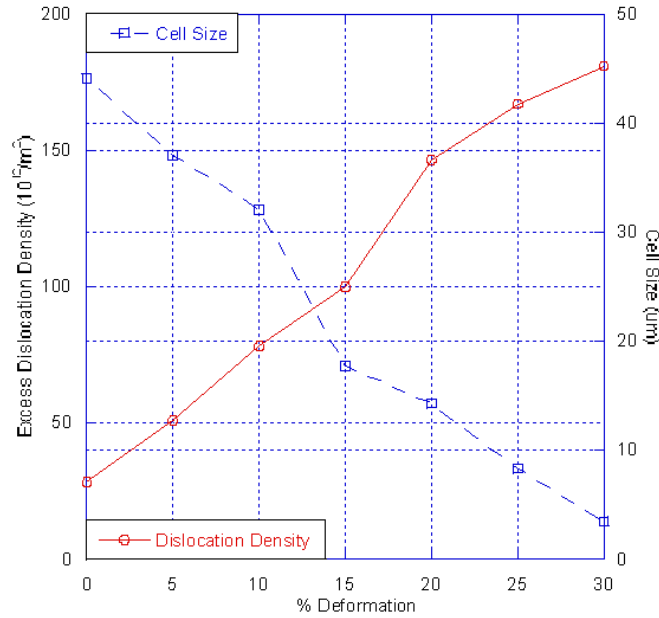


**Figure 3.4:** Excess dislocation density and dislocation cell size for each deformation step. Excess dislocation density increases with increasing deformation while dislocation cell size decreases.

steps with the highest density being in the higher Taylor Factor  $\{011\}$  and  $\{111\}$  grains as shown in Figure 3.6. The dislocation cell size with respect to crystal orientation does not follow a distinct trend and seems to be complicated by grain to grain interaction, while ultimately  $\{111\}$  grains deformed with the highest average lattice curvature, the  $\{001\}$  grains with an initially larger grain size than  $\{011\}$  grains showed a greater reduction rate in average cell size. At 15% deformation  $\{011\}$  density drops below that of the  $\{111\}$  density due to the local nature of the

data resulting in a lower number of data points for the specific deformation step. The prior deformation step and the subsequent step have significantly more data points due to grains rotating to {011} orientation to accommodate the local strain.

**Table 3.1:** Excess dislocation density evolution data for AA 1050 in channel die deformation from undeformed state through 30% deformation for sample 1 and sample 3 by orientation. Dislocation cell size evolution from undeformed through 30% deformation.

**Table 3.1 – Sample 1 & 3 Excess Dislocation Density**

	Deformation	EDD* ( $10^{12} \text{ m}^{-2}$ )	Cell Size ( $\mu\text{m}$ )	001 GND ( $10^{12} \text{ m}^{-2}$ )	011 GND ( $10^{12} \text{ m}^{-2}$ )	111 GND ( $10^{12} \text{ m}^{-2}$ )
Sample 1	0%	25.63	56.88	23.00	27.07	24.11
	0.5%	28.21	--	28.22	27.56	25.13
	1%	30.80	--	32.46	28.71	28.10
	1.5%	33.43	--	36.98	32.12	30.79
	2%	36.00	--	37.50	37.34	36.01
	2.5%	38.6	--	38.61	44.20	39.41
	3%	41.20	--	39.99	55.70	44.75
	4%	46.41	--	41.23	66.40	50.36
	5%	53.72	45.36	42.36	73.12	56.45
Sample 3	0%	28.51	44.17	25.75	30.75	26.5
	5%	51.26	37.10	34.08	82.75	58.12
	10%	78.47	32.11	65.92	100.67	95.57
	15%	100.25	17.76	95.24	115.36	131.29
	20%	146.87	14.26	105.88	189.72	176.2
	25%	167.01	8.39	124.75	202.89	189.22
	30%	181.23	3.54	135.66	215.01	200.99

\* - Excess dislocation density

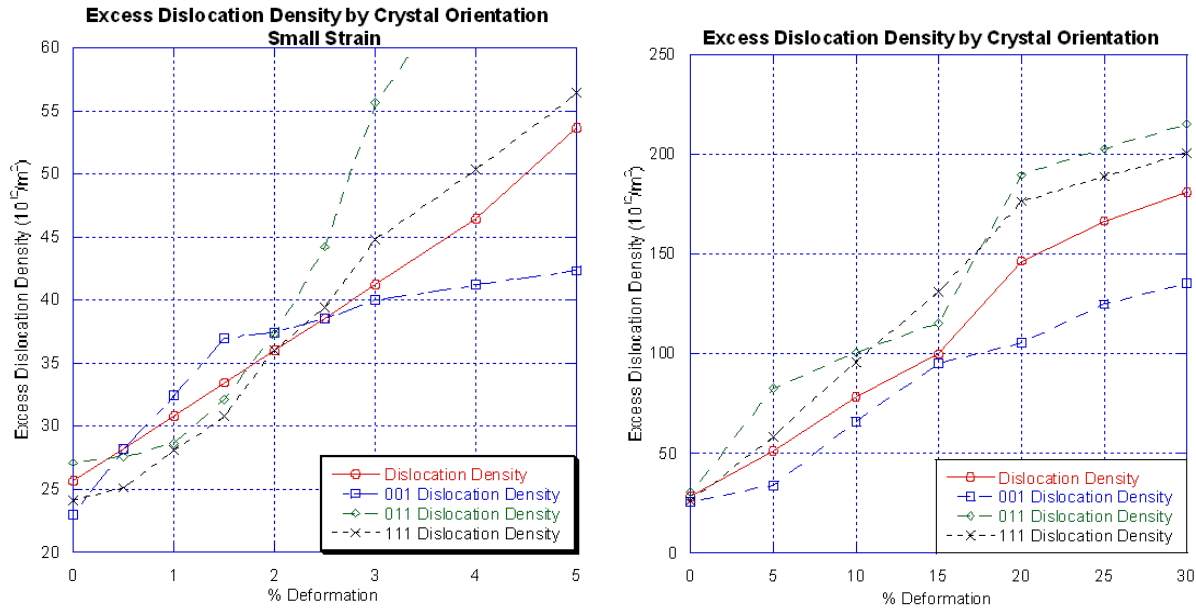


**Figure 3.5 and 3.6:** Excess dislocation density by orientation (left), initially the {001} increases at small strains more than the {011} and {111}, by a true strain of 0.025 the {011} and {111} have increased to a greater density than the {001}. Excess dislocation density by orientation (right), {011} and {111} show an increase in excess dislocation density faster than the {001} grains do for true strain steps of 0.05.

Once the excess dislocation density has been calculated it is possible to plot dislocation density in orientation space. Figure 3.7 shows the ODF of the undeformed material taken from the initial 2  $\mu\text{m}$  step size scan. This ODF appears significantly different than that shown in Figure 3.1 but is the same material in the same deformation state, it is simply a small subset of the grains from the initial ODF scan. The excess dislocation density was determined from these grains and can be plotted as a scalar value in orientation space resulting in a plot that shows the

orientations containing the highest excess dislocation density. Figure 3.8 shows the excess dislocation density plot after 20% compressive deformation. The undeformed excess dislocation

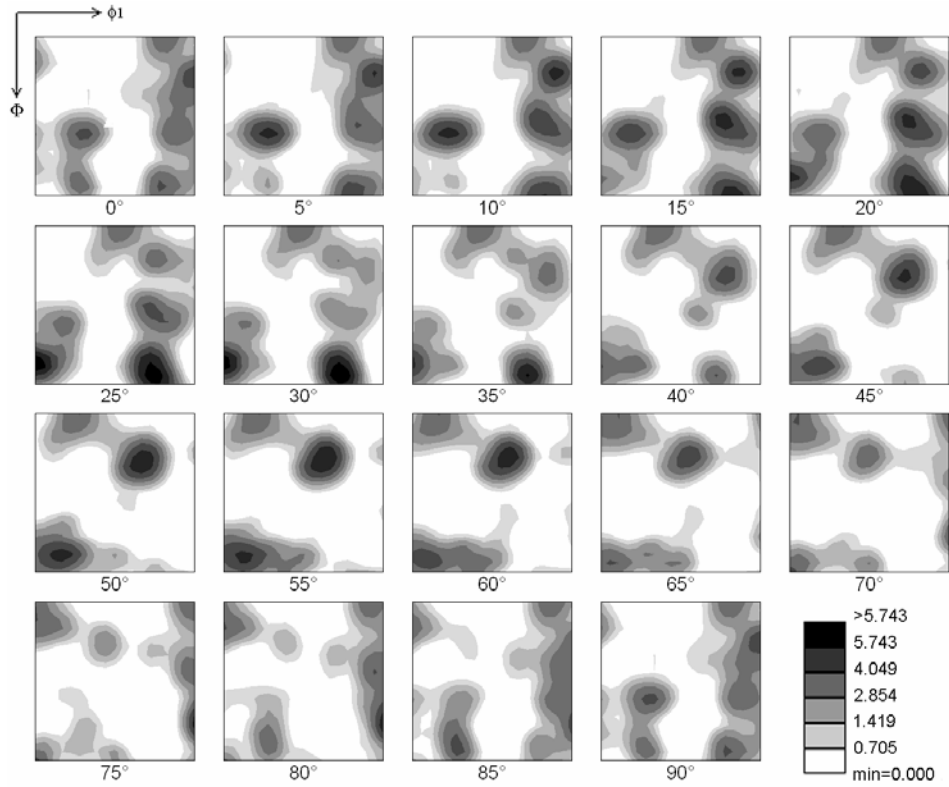


**Figure 3.7:** ODF of undeformed material of 2  $\mu\text{m}$  scan shows the texture for a local area only.

plot shows a fairly evenly distributed excess dislocation density across all orientations, which is to be expected in a recrystallized material. On the other hand, the 20% deformation excess dislocation plot shows a wide variety of behaviors with the highest intensity regions at an orientation near  $\{011\}\langle 122\rangle$ .



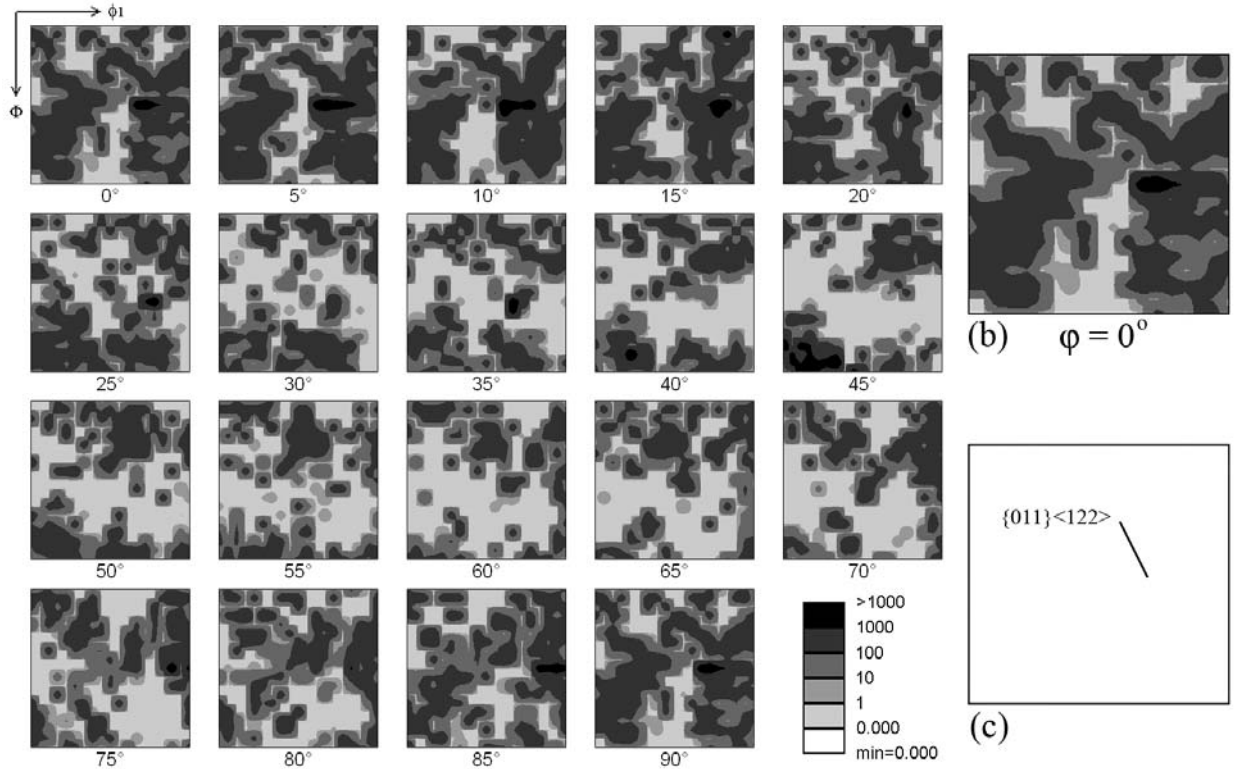


**Figure 3.8:** Excess dislocation density plotted in orientation space for 20% deformed material. The  $\{011\}\langle 122\rangle$  orientation shows the strongest dislocation density for the local area.

### 3.5 Discussion:

Evolution of excess dislocation content at a given position in the polycrystal depends upon the crystallite lattice orientation and initial local lattice curvature. However, the effects of grain to grain interactions, grain size effects, and other local and non-local material properties that are dependent upon processing could make this kind of determination far more complicated than it initially appears.

It should be noted that in the data presented above, all grains having a  $\{001\}$  pole aligned with the axis of compression in the channel die deformation are included in the plots as  $\{001\}$

grains. The same applies to  $\{110\}$  and  $\{111\}$  grains. This generalization was made because of the relatively few number of grains in the data sets used for this analysis. Granted that the Taylor factor can change significantly based on in-plane rotation of the grains. However, in the case of these orientations for plane strain deformation, the Taylor factor is generally smaller for  $\{001\}$  grains than for  $\{110\}$  or  $\{111\}$  grains regardless of in-plane orientation. Because of this, the results are generally applicable to grains of each pole orientation aligned with the compression axis even though the Taylor factor varies for grains included as having the same pole direction.

The excess dislocation density follows an appropriate trend showing that for small deformation steps the  $\{001\}$  grains initiate deformation as predicted by the Taylor factor. Both the  $\{011\}$  and  $\{111\}$  grains in the large deformation steps show the highest excess dislocation content which is introduced at larger strains and agrees with excess dislocation trends. As the dislocation density increases and dislocation-dislocation interactions become more prevalent, the grains begin to break up into volume elements to accommodate the macroscopic plastic strain through the operation of multiple slip systems. This results in the decreasing diameter of these volume elements and an increasing misorientation between each element. As these subgrains become more well-defined and orientation spreading occurs during deformation, grains of similar orientation should behave in a similar manner, ignoring grain to grain interactions. This would result in specific orientations of higher excess dislocation density which maybe plotted in orientation space for a visual representation of the data.

The Taylor factor for the orientation with the highest observed excess dislocation content,  $\{011\}[122]$ , is a quite high value of 4.62 and lies near the orientation  $\{011\}[011]$ , which has the highest Taylor factor possible (4.90) for this deformation gradient. It appears that on average,

the Taylor factor is a reasonable predictor of excess dislocation content. This is consistent with findings of other researchers who have used x-ray line broadening techniques, microhardness measurements, or TEM observations to obtain a measure of dislocation structure or stored energy in deformed polycrystals [17-20].

The excess dislocation density data plotted in orientation space for this paper was for a local region (570 x 1707  $\mu\text{m}$ ) of the material and is not representative of the entire material. For this type of plot to be representative of the bulk material and not a specific region, a large number of grains would need to be included (>1000 grains) [21]. Also it should be noted that to minimize “noise” in the excess dislocation density calculation, EBSD scan step sizes should be used that are approximately that of the subgrain or cell size diameter resulting in the misorientation between the subgrains to be calculated.

### **3.6 Conclusions:**

Two samples of Al 1050 were deformed in channel die compression to simulate idealized plain strain deformation seen in rolling. One sample was deformed in strain increments of  $\sim 0.0005$  while the other sample was deformed in strain increments of  $\sim 0.05$ . The small strain sample initially showed a greater incremental increase in  $\{001\}$  type grains, while the  $\{011\}$  and  $\{111\}$  type grains finally accumulated a greater number of excess dislocations at a true strain of 0.025. The large strain sample showed a continuation of this trend with  $\{011\}$  and  $\{111\}$  grains having the higher excess dislocation content. The strains from both samples that correlate to one another are within about 10% and show similar trends. The dislocation content was then plotted in orientation space to show the distribution of dislocations in order to identify the highest excess

dislocation density, which occurred at positions of highest Taylor Factor. For this data set, the highest excess dislocation density was measured in grains of  $\{011\}[122]$  orientation.

### 3.7 References:

- [1] D. Kuhlmann-Wilsdorf, N. Hansen, *Scripta Metall. Mater.* 25 (1991) 1557-1562.
- [2] W. Pantleon, *Acta Mater.* 46 (1998) 451-456.
- [3] W. Pantleon, *Mater. Sci. Eng. A234-236* (1997) 567-570.
- [4] W. Pantleon, *Mater. Sci. Eng. A319-321* (2001) 211-215.
- [5] D.P Field, H. Weiland, *Mat. Sci. Forum* 157-162 (1994) 1181-1188.
- [6] P. Trivedi, D.P. Field, H. Weiland, *Int. J. of Plasticity* 20 (2004) 459-476.
- [7] G. Winther, X. Huang, N. Hansen, *Acta Mater.* 48 (2000) 2187-2198.
- [8] A. Arsenlis, D.M. Parks, R. Becker, and V.V. Bulatov, *J. Mech. Phys. Sol.* 52 (2004) 1213-1246.
- [9] E. Kroner, *Appl. Mech. Rev.* 15 (1962) 599.
- [10] B. Bay, N. Hansen, D. Kuhlmann-Wilsdorf, *Mater. Sci. Eng. A113* (1989) 385-397.
- [11] D. Kuhlmann-Wilsdorf, *Mater. Sci. Eng. A113* (1989) 1-41.
- [12] N. Hansen, *Mater. Sci. Tech.* 6 (1990) 1039-1040.
- [13] D.A. Hughes, N. Hansen, *Mater. Sci. Tech.* 7 (1991) 544-553.
- [14] B. Bay, N. Hansen, D.A. Hughes, D. Kuhlmann-Wilsdorf, *Acta metal. mater.* 40 (1992) 205-219.
- [15] D.A. Hughes, N. Hansen, *Metall. Trans.* 24A (1993) 2021.
- [16] S. Panchanadeeswaran, R.D. Doherty, R. Becker, *Acta Mater.* 44 (1996) 1233-1262.

- [17] J.S. Kallend and Y.C. Huang, Proc. Seventh International Conference on Textures of Materials, Netherlands Soc. For Materials Science, 1984, pp. 783-786.
- [18] D.D. Sam and B.L. Adams, Metall. Trans. 17A (1986) 513-517.
- [19] S.F. Castro, J. Gallego, F.J.G. Landgraf, and H.-J. Kestenbach, Mat. Sci. Eng. A, 427 (2006) 301–305.
- [20] N. Hansen, X. Huang, W. Pantleon and G. Winther, Phil. Mag. 86 (2006) 3981-3994.
- [21] H.J. Bunge, Matls. Sci. Forum 157-162 (1994) 13-30.

## CHAPTER – 4

### **ORIENTATION DEPENDENCE OF DISLOCATION STRUCTURE EVOLUTION OF AA7050**

#### **4.1 Abstract:**

A well-organized dislocation structure forms in many polycrystalline metals during plastic deformation. This structure is often described qualitatively without regard to quantitative characterization. In this work, the evolution of dislocation structure in aluminum alloy 7050-T7451 is described by means of the excess dislocation density and by quantitative characterization of the cell structure as seen on a plane surface. The measurements were performed on a pseudo-internal surface of a split specimen deformed by channel die deformation. The results show a clear dependence of cell structure formation on orientation of the crystallite with respect to the imposed deformation gradient with the largest excess dislocation density occurring in grains of the  $\{001\}\langle 110\rangle$ ,  $\{112\}\langle 111\rangle$ , and  $\{112\}\langle 110\rangle$  orientations for plane strain deformation. Neighboring grain, precipitates, and non-local effects are shown to be of importance in the type of dislocation structures that evolve.

#### **4.2 Introduction:**

Aluminum alloy 7050-T7451 was developed in the 1970's to provide an alloy for the thick section airframe parts that require high yield strength, high toughness, and good corrosion resistance (bulkheads, wingspars, ect.). The manufacturing process, direct chill casting,

homogenization, hot rolling, solution heat treatment, quenching, stretching, and aging, result in a gradients of all the properties of the alloy across the thickness length scale [1-2]. This mechanical and physical anisotropy manifest themselves in through thickness by gradients in the crystallographic texture and a gradient in the second phase constituent particles ( $\text{Al}_2\text{CuMg}$ ,  $\text{MgZn}_2$ , ect.). The  $\text{Al}_2\text{CuMg}$  particles are brittle and easily crack and or debond from the aluminum matrix providing a site for a catastrophic failure to begin [3-4]. These particles also provide sites for, upon recrystallization, grains to nucleate forming a gradient in the grain size through the thickness of the plate. Recrystallized grains are typically much larger with the majority occurring in the quarter plane of the plate (T/4). Nanoscale precipitates harden the alloy system, but do not contribute to the material strengthening anisotropy because the matrix and precipitates share many of the same habit planes [5]. But due to constituent concentration gradients there can be variations on the number of particles present in the through thickness of the material.

Evolution of dislocation structures through interactions of dislocations with particles, solutes, and other dislocations controls the deformation response of polycrystalline aluminum alloys. As deformation increases in a material, grains begin to break into volume elements that decrease in size with increasing strain. These volume elements are characterized by two different types of boundaries, incidental dislocation boundaries and geometrically necessary boundaries. Incidental dislocation boundaries (IDB) form by the random trappings of dislocations and geometrically necessary boundaries (GNB) form between regions with one or more different operating slip systems to accommodate the accompanying difference in lattice rotation [6]. These boundaries contain both statistically stored dislocations (redundant,  $+b -b$ ), which do not contribute significantly to a net lattice rotation, and excess dislocations (non-redundant, often



termed geometrically necessary dislocations) that contribute to the net lattice rotation [7-9]. It has been observed by various authors that the character of dislocation structures formed is a function of the lattice orientation with respect to the imposed deformation gradient [10-12]. The presence of these deformation gradients in a material give rise to a lattice rotation  $\theta$  and a net Burgers vector resulting in a rotation. The purpose of the present work is to obtain experimental data of dislocation structure evolution, in support of the development of a three dimensional crystal plasticity model to describe the deformation behavior of aluminum alloys. Basic to this model is an explicit evolution of dislocation density on all slip systems and the concept that the material behavior is controlled by the motion and interaction of excess dislocations [13]. The evolution of dislocation density depends on the divergence of dislocation fluxes associated with the inhomogeneous nature of plasticity in crystals [14]. Dislocation structure evolution during cold deformation of FCC polycrystals has been extensively investigated over the past couple of decades with primary emphasis on a qualitative description of the evolving structures and their relation to mechanical properties [15-20].

#### **4.3 Experimental Details:**

Aluminum alloy 7050-T7451 was obtained as industrially hot-rolled thick plate (~100 mm thick). Two samples were taken from the quarter plane (t/4 section) of the material and machined to final dimensions of 10 x 20 x 7.5 mm. No further heat treatment was conducted leaving the material in the as received condition. In the present experiments a channel die is used to simulate cold rolling of aluminum. This die imposes a nominally plane strain deformation gradient on the metal similar to that experienced by the aluminum passing through a rolling mill. To avoid problems associated with frictional conditions on the surfaces, the analysis surface is a

pseudo-internal interface wherein the specimen is split in two and the mating surfaces are prepared by a fine metallographic polish before deformation [21]. This surface is suitable for characterization by electron backscatter diffraction at various steps through the deformation process because it is protected from the majority of the shear deformation characteristic of the specimen surfaces in channel die deformation. Two samples were deformed at room temperature by channel die compression in true strain increments of  $\sim 0.05$  at a strain rate of  $\sim 5.5 \times 10^{-3} \text{ s}^{-1}$ , while the other two samples were deformed in true strain increments of  $\sim 0.005$  at a strain rate of  $\sim 5.5 \times 10^{-3} \text{ s}^{-1}$ . This form of plain strain deformation was used to impose the idealized deformation seen in rolling. TEFLON film was placed between the two samples and the samples and the die walls to prevent galling. At a strain of  $\sim 0.10$  the samples that were deformed in strain increments of  $\sim 0.05$  were reduced in size to  $10 \times 15 \times 7.5 \text{ mm}$  to lower the force needed to deform the material. However, due to the load capacity of the testing system the maximum attainable strain in these tests was a strain of  $\sim 0.15$ .

EBSA analysis was performed using a Schottky source field-emission scanning electron microscope. Prior to channel die deformation an  $80 \text{ mm}^2$  area was scanned using a  $40 \text{ }\mu\text{m}$  step size to collect the initial texture. All subsequent scans were of the same  $0.94 \text{ mm}^2$  area with a  $2 \text{ }\mu\text{m}$  step size. Scans of  $0.2 \text{ }\mu\text{m}$  step size were taken within the  $0.94 \text{ mm}^2$  area to confirm the dislocation cell size. The scans were centered in the middle of the sample to minimize edge effects and any anomalous effects created by the punch or the die. The smaller step size was used in this area to obtain local information about point to point misorientation within grains allowing for calculation of excess dislocation density, dislocation cell size, and local orientation distribution of dislocations. Black regions in orientation images are regions with low confidence index ( $\text{CI} < 0.2$ ) data. The black regions in excess dislocation density images are either bad data or

regions of low dislocation density. Misorientations of  $5^\circ$  or greater are ignored, so data points along grain boundaries generally have a low apparent dislocation density. For the excess dislocation content and Taylor factor plotted in orientation space the same  $80 \text{ mm}^2$  area was scanned to accurately represent the bulk material. Scans were completed at  $15 \mu\text{m}$ .

The data analysis was performed with in house software that had been modified to include the calculation of the dislocation density tensor. The software was set with the following parameters: grain tolerance angle –  $2^\circ$ , minimum grain size – 5 steps. All averages are number averages which translate directly to averages of the grain area owing to the principle of DeLesse and the measurement strategy where data points are taken over a regular hexagonal array. Taylor factors for the given orientations were calculated using the family of active slip systems for FCC metals ( $\{111\}\langle 1-10\rangle$ ) and the plane strain deformation gradient;  $\sigma_{xx} = 1$ ,  $\sigma_{zz} = -1$ ,  $\sigma_{yy} = \sigma_{xy} = \sigma_{xz} = \sigma_{yz} = 0$ .

#### 4.4 Results

The as received material was in the form of 100 mm thick hot rolled plate. The texture of the AA 7050 samples contains a combination of cube texture and an fcc rolling texture, showing a weak  $\beta$  fiber as show in the orientation distribution function (ODF) in Figure 4.1. Scatter occurs as the  $\beta$  fiber approaches the rotated cube orientation  $\{001\}\langle 110\rangle$  along with the rotated cube orientation while no  $\{111\}\langle uvw\rangle$  component is observed in  $\varphi_2 = 45^\circ$  [22]. In addition to the shear texture there is a strong cube orientation component present  $\{001\}\langle 100\rangle$  and brass component  $\{110\}\langle 112\rangle$  as shown in  $\varphi_2 = 0^\circ$ . Figure 4.2 shows the progression of orientation images obtained from a given area of one of the samples from the undeformed state to a state of

15% reduction. The undeformed orientation image shows a hot-rolled structure with a large variation in dislocation

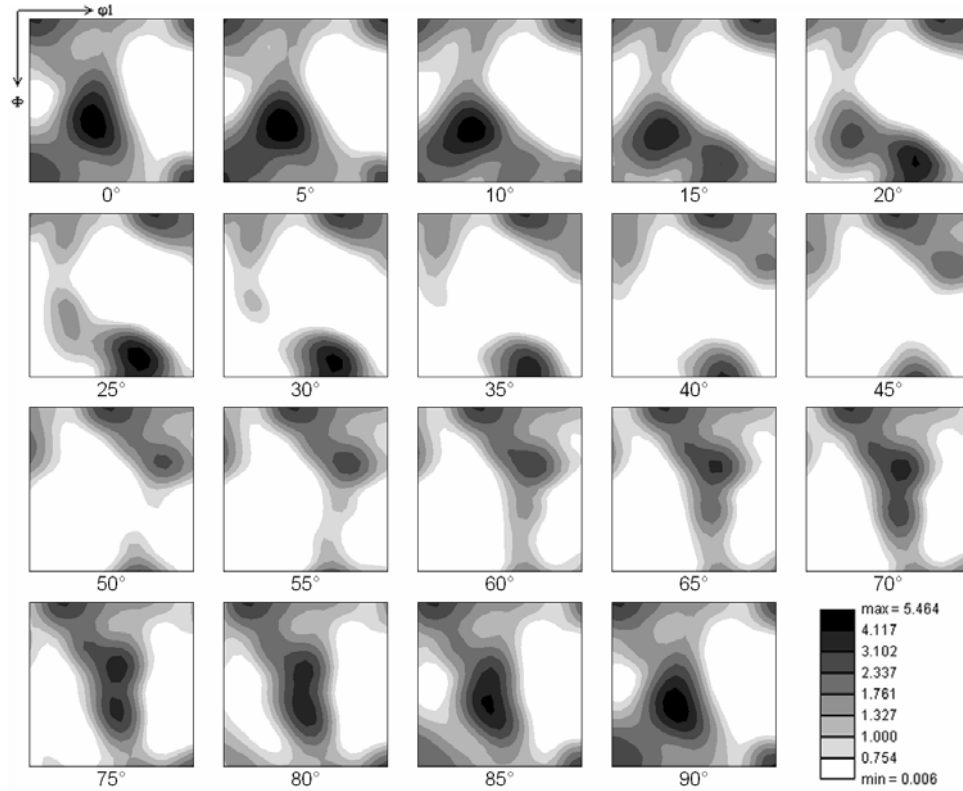


**Figure 4.1:** ODF of undeformed material contains a combination of cube texture and fcc rolling texture, showing a weak  $\beta$  fiber. Scatter occurs as the  $\beta$  fiber approaches the rotated cube orientation  $\{001\}\langle 110\rangle$  along with the rotated cube orientation while no  $\{111\}\langle uvw\rangle$  component is observed in  $\varphi_2 = 45^\circ$ .

cell size along the grain boundaries due to the manufacturing process of the sample. There is a significant amount of lattice curvature present in the undeformed material. The Taylor factor was calculated for  $\{001\}\langle 100\rangle$  orientations to be 2.22 for the given deformation state, while the  $\{011\}\langle 1-12\rangle$  was 3.07 and the  $\{111\}\langle 01-1\rangle$  grain had a Taylor factor of 2.86. This would

indicate that the  $\{011\}$  and  $\{111\}$  grains should not deform until the  $\{001\}$  grains had hardened sufficiently to initiate slip in the grains of higher Taylor factor. Ultimately the higher Taylor

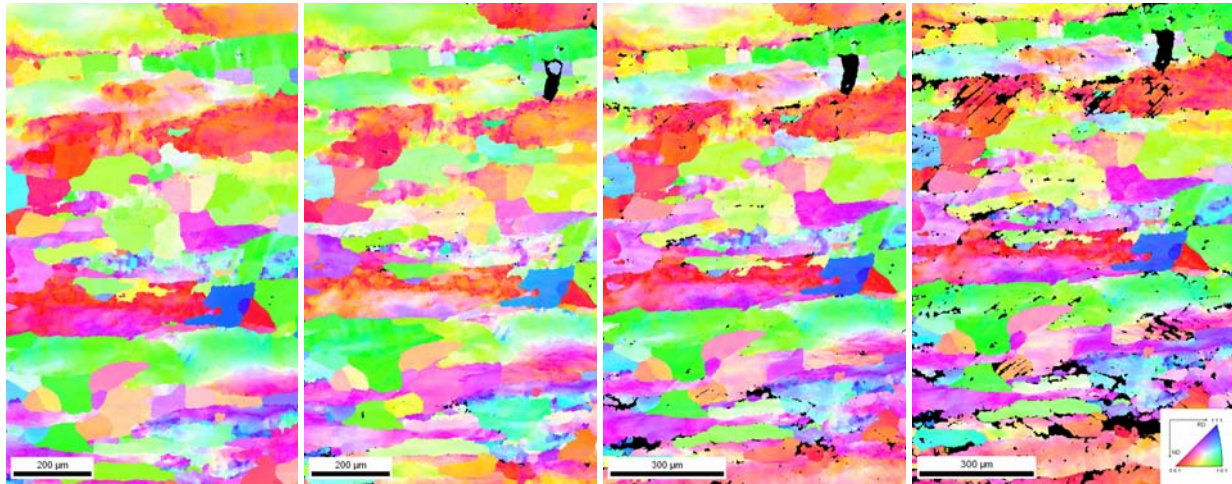


**Figure 4.2:** Orientation images, from left to right, of undeformed (a), 5% (b), 10% (c), and 15% (d) reduction.

factor grains would have a higher excess dislocation density due to the increased slip necessary for unit strain in these grains. On the other hand the  $\{001\}$  grains should initially deform easily resulting in a higher excess dislocation density but as the samples proceed through large deformation steps the excess dislocation density should not increase as rapidly as the  $\{011\}$  and  $\{111\}$  type grains. This is because the low Taylor factor means that these grains are “soft” in relation to the neighboring structure and will deform first, resulting in an increased dislocation density. As these harden due to the cold work, the grains with increased Taylor factor will deform. Because of the increased Taylor factor these require more dislocation motion per unit strain to deform, therefore the density will increase at a more rapid rate than in these grains with a lower Taylor factor. This trend was observed experimentally when the excess dislocation

density was calculated. Neighboring grains influence this behavior by constraints imposed upon deformation of softer grains by load shielding from grains of higher Taylor factor, resulting in dislocation density evolution to be less predictable for these regions.

Figure 4.3 shows the excess dislocation density maps generated from the same data represented in the orientation images shown in Figure 4.2. White areas are regions of high excess dislocation density while black regions are grain boundaries or data filtered out by the software. The gray scale indicates black for regions of excess dislocation density less than  $10^{11} \text{ m}^{-2}$  to white for densities of  $10^{15} \text{ m}^{-2}$  on a linear scale. Regions of highest density occur in the  $\{112\}\langle uvw \rangle$  orientations in the undeformed material and continue to have the highest densities through the deformation process. Grain to grain interaction produces local regions of high dislocation densities that appear planar and are parallel to the RD.

While in a previous study [23] the samples were recrystallized and comparatively dislocation free,  $2 \times 10^{13} \text{ m}^{-2}$ , these samples have been hot rolled and aged resulting in a highly deformed and polygonized initial structure with wide variations in dislocation cell sizes, especially along grain boundaries. Initially the hard grains deform very little while imposing greater deformation on the soft grains. As the excess dislocation density increases there is particle ( $\text{MgZn}_2$ ) – dislocation interaction and dislocation-dislocation interaction, resulting in an increasingly well-defined grain substructure. Subsequent dislocation cell sizes decreased with each deformation step and the excess dislocation density increased as shown in Figure 4.4 and Table 4.1.

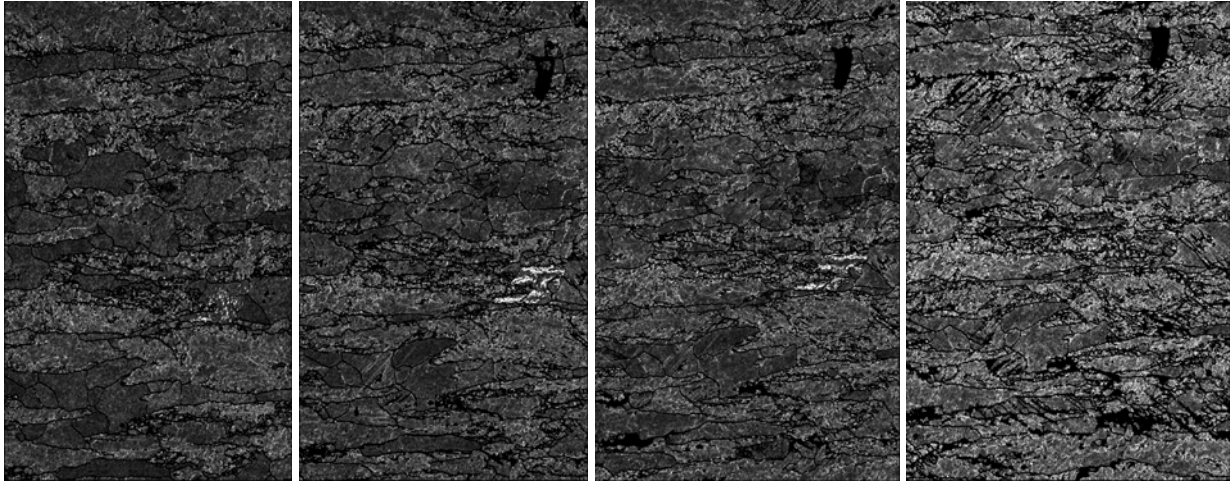


**Figure 4.3:** Excess dislocation density maps for the orientation images shown in Figure 2. Black areas are the lowest density ( $10^{11} \text{ m}^{-2}$ ) areas and regions of low confidence data while the lighter areas are the regions of highest excess dislocation density ( $10^{15} \text{ m}^{-2}$ ).

With respect to specific orientations for small deformation steps, incrementally the  $\{001\}$  grains increase the most through a true strain of 0.05. At a true strain of 0.05 through 0.1 the  $\{011\}$  grains significantly increase in excess dislocation content shown in Figure 4.5. After which the excess dislocation content does not significantly increase in any specific orientation shown. The dislocation cell size with respect to crystal orientation does not follow a distinct trend and seems to be complicated by the initial condition of the alloy.

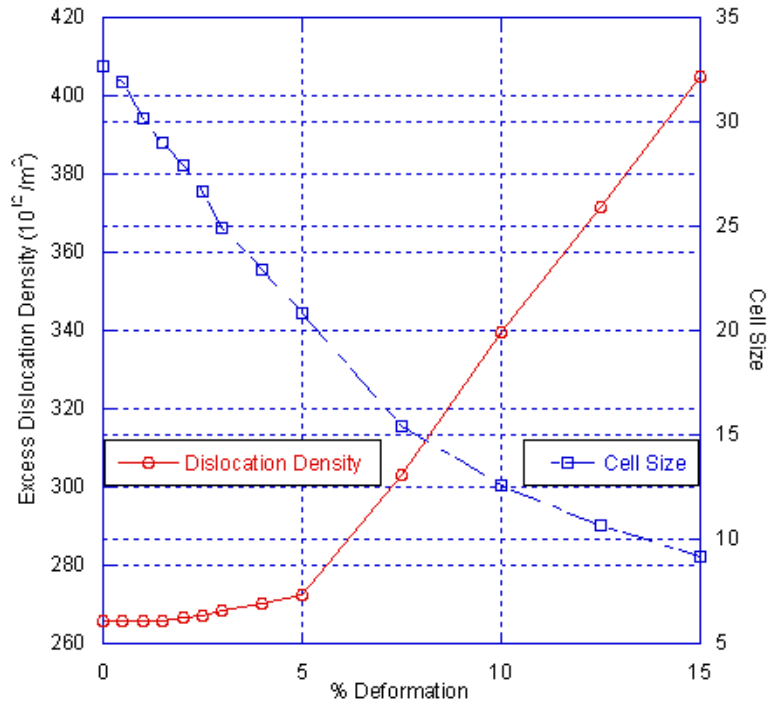


**Figure 4.4:** Excess dislocation density and dislocation cell size for each deformation step. excess dislocation density increases with increasing deformation while dislocation cell size decreases.

With respect to specific orientations for small deformation steps, incrementally the  $\{001\}$  grains increase the most through a true strain of 0.05. At a true strain of 0.05 through 0.1 the  $\{011\}$  grains significantly increase in excess dislocation content shown in Figure 4.5. After which the excess dislocation content does not significantly increase in any specific orientation shown. The dislocation cell size with respect to crystal orientation does not follow a distinct trend and seems to be complicated by the initial condition of the alloy.



**Table 4.1:** Excess dislocation density evolution data for AA 7050 T7451 in channel die deformation from undeformed state through 15% deformation by orientation. Dislocation cell size evolution from undeformed through 15% deformation.

**Table 4.1 – Sample 1 Excess Dislocation Density**

	Deformation	EDD*	Cell Size	001 GND	011 GND	111 GND
		( $10^{12} \text{ m}^{-2}$ )	( $\mu\text{m}$ )	( $10^{12} \text{ m}^{-2}$ )	( $10^{12} \text{ m}^{-2}$ )	( $10^{12} \text{ m}^{-2}$ )
Sample 1	0%	265.78	32.64	146.73	683.93	224.42
	0.5%	265.64	31.93	147.62	682.41	225.25
	1%	265.63	30.13	150.12	683.44	225.95
	1.5%	265.70	28.90	154.23	684.32	227.04
	2%	266.83	27.88	158.36	684.98	228.26
	2.5%	267.22	26.63	161.32	684.33	229.49
	3%	268.41	24.90	164.58	685.66	232.13
	4%	270.23	22.89	170.89	685.22	235.33
	5%	272.48	20.82	175.17	684.81	238.09
	7.5%	302.98	15.45	182.67	735.40	239.98
	10%	339.38	12.61	192.69	798.16	241.61
	12.5%	370.50	10.67	195.99	813.32	253.01
	15%	405.13	9.16	203.38	822.26	261.61

\* - Excess dislocation density

Once the excess dislocation density has been calculated it is plotted in orientation space from data generated from orientation images. The excess dislocation density was determined from these grains and can be plotted as a scalar value in orientation space resulting in a plot that

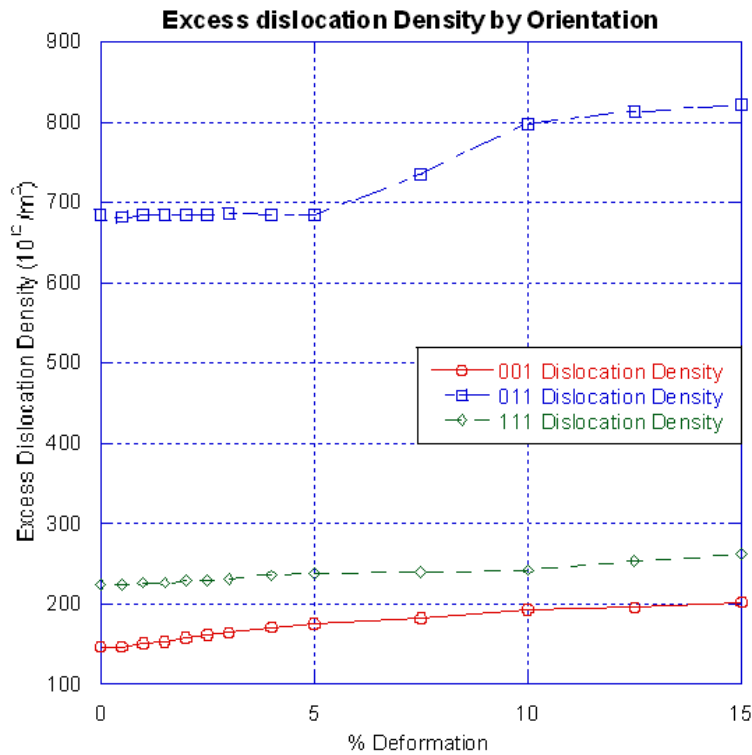


**Figure 4.5:** Excess dislocation density by orientation, initially the {011} start with a very high dislocation density due to the manufacturing processes. Both {001} and {111} grains show a fairly linear increase throughout the deformation process, while the {011} jump significantly after 5% deformation.

shows the orientations containing the highest excess dislocation density. Figure 4.6 shows the excess dislocation density plots from the undeformed state through 15% deformation. The undeformed excess dislocation plot shows a fairly evenly distributed excess dislocation density across all orientations, with a slightly higher density at the {112}<110> which is visible in the  $\varphi_2 = 65^\circ$  and  $\varphi_2 = 45^\circ$  and {112}<111> visible in  $\varphi_2 = 45^\circ$ . As deformation progresses to 5% dislocation density rapidly increases in the rotated cube orientation {001}<110>.

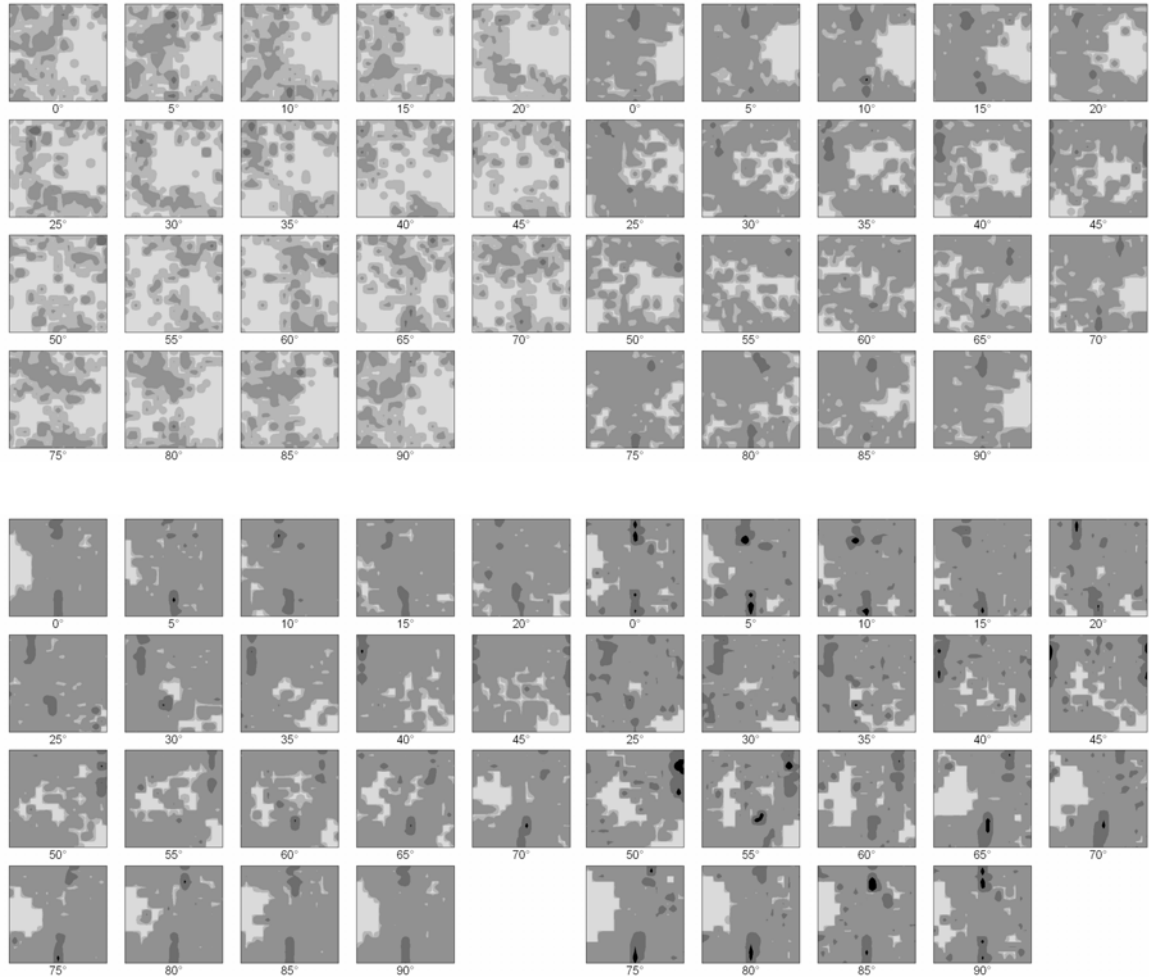


**Figure 4.6:** Excess dislocation density plotted in ODF space. Initially fairly even distribution with a slight peak at an orientation of  $\{110\}\langle 111\rangle$  in the undeformed state. As deformation increases excess dislocation density increases steadily along the  $\{111\}\langle uvw\rangle$  fiber.

The next step in analyzing the results was to plot the Taylor factor in orientation space as a scalar value, the same process as plotting the excess dislocation content in orientation space, to observe any correlation between excess dislocation content and Taylor factor. Figure 4.7 shows the Taylor factors plotted in orientation space from the same maps that the texture ODF and excess dislocation content plotted in orientation space were calculated from, only the

undeformed plot is shown. There appears to be a strong correlation between orientations with a Taylor factor  $> 4.0$  and high excess dislocation content. While a weaker correlation exists between orientations with Taylor factors  $< 3.0$  and lower excess dislocation content in the undeformed material. The Taylor factor along the  $\beta$ -fiber (also along rolling texture) is  $> 3.5$  and is greater than the surrounding orientations and is in agreement with the excess dislocation plots.

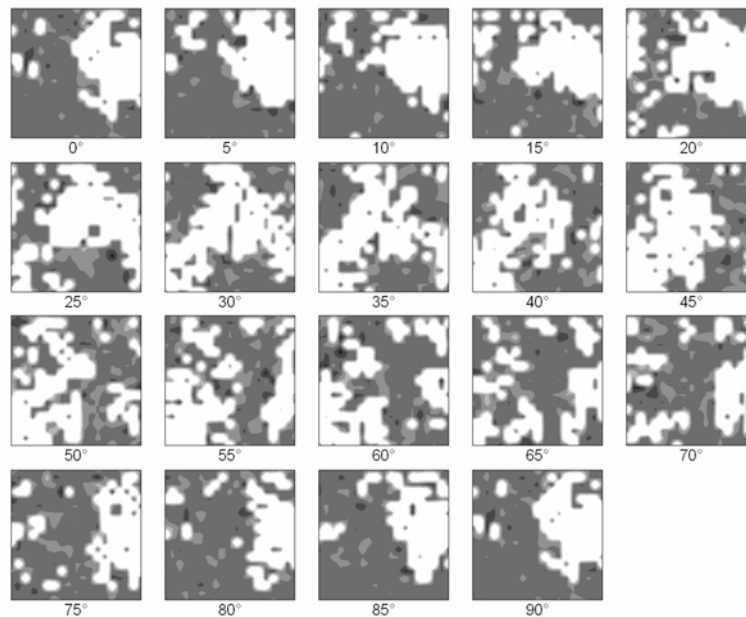


**Figure 4.7:** Taylor factor plotted in orientation space for the undeformed material. A good correlation between regions of high Taylor factor  $> 4.0$  and regions of high excess dislocation density exist.

#### 4.5 Discussion:

Evolution of excess dislocation content at a given position in the polycrystal depends upon the crystallite lattice orientation and initial local lattice curvature. However, the effects of grain to grain interactions, grain size effects, and other local and non-local material properties

that are dependent upon processing could make this kind of determination far more complicated than it initially appears.

It should be noted that in the data presented above, all grains having a  $\{001\}$  pole aligned with the axis of compression in the channel die deformation are included in the plots as  $\{001\}$  grains. The same applies to  $\{110\}$  and  $\{111\}$  grains. The Taylor factor can change significantly based on in-plane rotation of the grains. However, in the case of these orientations for plane strain deformation, the Taylor factor is generally smaller for  $\{001\}$  grains than for  $\{110\}$  or  $\{111\}$  grains regardless of in-plane orientation. Because of this, the results are generally applicable to grains of each pole orientation aligned with the compression axis even though the Taylor factor varies for grains included as having the same pole direction.

The excess dislocation density follows an appropriate trend showing that for small deformation steps the  $\{001\}$  grains initiate deformation as predicted by the Taylor factor. The  $\{011\}$  and  $\{111\}$  grains in the large deformation steps show the highest excess dislocation content which is introduced at larger strains and agrees with excess dislocation trends. As the dislocation density increases and dislocation-dislocation interactions become more prevalent, the grains continue to break up further into volume elements to accommodate the macroscopic plastic strain through the operation of multiple slip systems. This results in a decreasing diameter of these volume elements and an increasing misorientation between each element. As these subgrains become more well-defined and orientation spreading occurs during deformation, grains of similar orientation should behave in a similar manner, ignoring grain to grain interactions. This would result in specific orientations of higher excess dislocation density which may be plotted in orientation space for a visual representation of the data.

The Taylor factor for the orientation with the highest observed excess dislocation content,  $\{011\}\langle 122\rangle$ , is a quite high value of 4.30 and lies near the orientation  $\{011\}\langle 011\rangle$ , which has the highest Taylor factor possible (4.90) for this deformation gradient. It appears that on average, the Taylor factor is a reasonable predictor of excess dislocation content at this strain level. This is consistent with findings of other researchers who have used X-ray line broadening techniques, microhardness measurements, or TEM observations to obtain a measure of dislocation structure or stored energy in deformed polycrystals [24-27].

The excess dislocation density data plotted in orientation space for this paper was for the bulk material (4.25 x 9.25 mm) and is representative of the entire material. For this type of plot to be representative of the bulk material a large number of grains would need to be included (>1000 grains) [28]. Also it should be noted that to minimize “noise” in the excess dislocation density calculation, EBSD scan step sizes should be used that are approximately that of the subgrain or cell size diameter resulting in the misorientation between the subgrains to be calculated.

#### **4.6 Conclusions:**

Two samples of AA 7050 were deformed in channel die compression to simulate idealized plain strain deformation seen in rolling. One sample was deformed in strain increments of  $\sim 0.005$  while the other sample was deformed in strain increments of  $\sim 0.05$ . The small strain sample initially showed a greater incremental increase in  $\{001\}$  type grains, while the  $\{011\}$  type grains surpassed them in incremental increase in the number of excess dislocations at a true strain of 0.05. The large strain sample showed a continuation of this trend with the  $\{011\}$  grains

having a higher incremental increase in excess dislocation content, while the  $\{111\}$  grains do not show much incremental increase in excess dislocation content throughout the small or large strain sample. The strains from both samples that correlate to one another are within about 5% and show similar trends. The excess dislocation content was then plotted in orientation space to show the distribution of dislocations in order to identify the highest excess dislocation density, which occurred near the positions of highest Taylor Factor, also plotted in orientation space. For the AA 7050 data sets, the highest excess dislocation density was measured in grains of the  $\{001\}\langle 110\rangle$ ,  $\{112\}\langle 111\rangle$ , and  $\{112\}\langle 110\rangle$  orientations on the order of  $10^{15} \text{ m}^{-2}$ .

#### 4.7 References:

- [1] M.C Flemings, G.E. Nereo, Trans. AIME, 242 (1968) 50-55.
- [2] A.J. Beaudoin, W.A. Cassada, Proc. TMS Spring Meeting, (1998).
- [3] R.H. Srone, J.A. Psioda, Met. Trans. A, 6A (1975) 668-670.
- [4] N.U. Deshpande, Metal. Trans. A, 29A (1998) 1191-1201.
- [5] J. Gjornes, C.J. Simensen, Acta Met. 18 (1970) 881.
- [6] D. Kuhlmann-Wilsdorf, N. Hansen, Scripta Metall. Mater. 25 (1991) 1557-1562.
- [7] W. Pantleon, Acta Mater. 46 (1998) 451-456.
- [8] W. Pantleon, Mater. Sci. Eng. A234-236 (1997) 567-570.
- [9] W. Pantleon, Mater. Sci. Eng. A319-321 (2001) 211-215.
- [10] D.P Field, H. Weiland, Mat. Sci. Forum 157-162 (1994) 1181-1188.
- [11] P. Trivedi, D.P. Field, H. Weiland, Int. J. of Plasticity 20 (2004) 459-476.
- [12] G. Winther, X. Huang, N. Hansen, Acta Mater. 48 (2000) 2187-2198.
- [13] A. Arsenlis, D.M. Parks, R. Becker, and V.V. Bulatov, J. Mech. Phys. Sol, 52 (2004) 1213-1246.
- [14] E. Kroner, Appl. Mech. Rev. 15 (1962) 599.
- [15] B. Bay, N. Hansen, D. Kuhlmann-Wilsdorf, Mater. Sci. Eng. A113 (1989) 385-397.
- [16] D. Kuhlmann-Wilsdorf, Mater. Sci. Eng. A113 (1989) 1-41.



- [17] N. Hansen, *Mater. Sci. Tech.* 6 (1990) 1039-1040.
- [18] D.A. Hughes, N. Hansen, *Mater. Sci. Tech.* 7 (1991) 544-553.
- [19] B. Bay, N. Hansen, D.A. Hughes, D. Kuhlmann-Wilsdorf, *Acta metal. mater.* 40 (1992) 205-219.
- [20] D.A. Hughes, N. Hansen, *Metall. Trans.* 24A (1993) 2021.
- [21] S. Panchanadeeswaran, R.D. Doherty, R. Becker, *Acta Mater.* 44 (1996) 1233-1262.
- [22] O. Engler, M.-Y Huh, C.N. Tome, *Metall. Mater. Trans. A*, 31A (2000) 2299-2315.
- [23] C.C. Merriman, D.P. Field, P. Trivedi, *Metall. Mater. Trans. A*
- [24] J.S. Kallend and Y.C. Huang, *Proc. Seventh International Conference on Textures of Materials*, Netherlands Soc. For Materials Science, 1984, pp. 783-786.
- [25] D.D. Sam and B.L. Adams, *Metall. Trans.* 17A (1986) 513-517.
- [26] S.F. Castro, J. Gallego, F.J.G. Landgraf, and H.-J. Kestenbach, *Mat. Sci. Eng. A*, 427 (2006) 301–305.
- [27] N. Hansen, X. Huang, W. Pantleon and G. Winther, *Phil. Mag.* 86 (2006) 3981-3994.
- [28] H.J. Bunge, *Matls. Sci. Forum* 157-162 (1994) 13-30.

## **CHAPTER – 5**

### **CONCLUSIONS**

This chapter summarizes the major points of emphasis in the present thesis, and highlights the important conclusions.

- The improvement of characterization techniques to define and image the local orientation gradients in 2-D and 3-D for deformed single and polycrystalline samples. Characterization techniques were applied to two AA 7050 polycrystalline samples and copper single crystal sample that were deformed to understand the development of local orientation gradient and the effects of step size of excess dislocation density.
- The first sample of Al 7050 was deformed in channel die compression to a 5% height reduction. The sample had four serial sections of EBSD data collected through OIM and FIB milling. An average 3-D excess dislocation density of  $1786 \times 10^{12} \text{ m}^{-2}$  was calculated while the average 2-D density was  $946 \times 10^{12} \text{ m}^{-2}$ . An AA 7075 sample dataset collected from tensile fatigue specimen with 29 serial sections showed an average 3-D excess dislocation density of  $3063 \times 10^{12} \text{ m}^{-2}$  and an average 2-D density of  $1924 \times 10^{12} \text{ m}^{-2}$ .
- The second AA 7050 sample and a single crystal copper dataset were used to show the influence of step size of the excess dislocation density. It was observed as the step size

was decreased (i.e.  $1\ \mu\text{m} \rightarrow 0.2\ \mu\text{m}$ ) the excess dislocation density increased following a power law curve. Also for 3-D calculations the spacing between serial sections has the same effect as increasing or decreasing the step size. The same trends were observed in polycrystalline and single crystal datasets.

- Two samples of Al 1050 were deformed in channel die compression to simulate idealized plain strain deformation seen in rolling. One sample was deformed in strain increments of  $\sim 0.005$  while the other sample was deformed in strain increments of  $\sim 0.05$ . The small strain sample initially showed a greater incremental increase in  $\{001\}$  type grains, while the  $\{011\}$  and  $\{111\}$  type grains finally accumulated a greater number of excess dislocations at a true strain of 0.025. The large strain sample showed a continuation of this trend with  $\{011\}$  and  $\{111\}$  grains having the higher excess dislocation content.
- The dislocation content was then plotted in orientation space to show the distribution of dislocations in order to identify the highest excess dislocation density, which occurred at positions of highest Taylor factor. For this data set, the highest excess dislocation density was measured in grains of  $\{011\}\langle 122 \rangle$  orientation.
- Two samples of AA 7050 were deformed in channel die compression. One sample was deformed in strain increments of  $\sim 0.005$  while the other sample was deformed in strain increments of  $\sim 0.05$ . The small strain sample initially showed a greater incremental increase in  $\{001\}$  type grains, while the  $\{011\}$  type grains surpassed them in incremental increase in the number of excess dislocations at a true strain of 0.05. The large strain

sample showed a continuation of this trend with the {011} grains having a higher incremental increase in excess dislocation content, while the {111} grains do not show much incremental increase in excess dislocation content throughout the small or large strain sample.

- The excess dislocation content and Taylor factor were plotted in orientation space to show the distribution of excess dislocations in order to identify the highest excess dislocation density, which occurred near the positions of highest Taylor factor. For the AA 7050 data sets, the highest excess dislocation density was measured in grains of the {001}<110>, {112}<111>, and {112}<110> orientations on the order of  $10^{15} \text{ m}^{-2}$ . The Taylor factor in orientation space appears to be a good predictor of orientations that will evolve the highest excess dislocation densities.

## **CHAPTER – 6**

### **SUGGESTIONS FOR FUTURE WORK**

The current study focused on the improvement of characterization techniques involving the indirect observation of dislocations. Through this a lower bound calculation of the excess dislocation density is possible in 2-D (planar sections) and 3-D (serial sections). The 2-D and 3-D dislocation density dependence on step size needs to be investigated further while determining the best method for excluding the step size from the dislocation density through data smoothing or another method.

Correlate the results of the current study with results seen in TEM samples in the same deformation states and alloys. Investigate the orientation dependence of dislocation structure evolution by observing the cell structure and substructure in specific crystal orientations in single crystal samples. Understand the microstructural response and relationship of dislocation evolution and the orientation dependence of this evolution based on Taylor factor.

AA 7050 and AA 7075 fatigue specimens to observe the fatigue response of materials in use on military and civilian airframes using both SEM and TEM techniques.

## APPENDIX

### A. 3-D EXCESS DISLOCATION DENSITY CALCULATION C++ CODE

Dataset.h

```
void SetPoint(CDatapoint dp);  
  
void SetPoint(int col, int row, CDatapoint dp);  
  
void SetIQ(float iq);  
  
void SetIQ(int col, int row, float iq);  
  
VECTORDATAPOINT GetNeighbors(void);
```

Dataset.cpp

```
void CDataset::SetPoint(CDatapoint dp)  
{  
    int pos = CurrentPos();  
    if(pos>=0)  
        m_DatapointVector[pos] = dp;  
}  
  
void CDataset::SetPoint(int col, int row, CDatapoint dp)  
{  
    int pos = CalcPos(col,row);
```

```

        if(pos>=0)

            m_DatapointVector[pos] = dp;

    }

void CDataset::SetIQ(float iq)

{

    int pos = CurrentPos();

    if(pos >= 0)

        m_DatapointVector[pos].iq = iq;

}

void CDataset::SetIQ(int col, int row, float iq)

{

    int pos = CalcPos(col,row);

    if(pos >= 0)

        m_DatapointVector[pos].iq = iq;

}

VECTORDATAPOINT CDataset::GetNeighbors(void)

{

    VECTORDATAPOINT neighbors;

    // Get points to the left and right of the current point

```

```

if(CalcPos(GetCol()-1,GetRow()) >= 0)

    neighbors.push_back(GetPoint(GetCol()-1,GetRow()));

if(CalcPos(GetCol()+1,GetRow()) >= 0)

    neighbors.push_back(GetPoint(GetCol()+1,GetRow()));

// Get points up and down from the current point

if(GetGridType() == GRID_HEX)

{

    if(CalcPos(GetCol(),GetRow()-2) >= 0)

        neighbors.push_back(GetPoint(GetCol(),GetRow()-2));

    if(CalcPos(GetCol(),GetRow()+2) >= 0)

        neighbors.push_back(GetPoint(GetCol(),GetRow()+2));

}

else

{

    if(CalcPos(GetCol(),GetRow()-1) >= 0)

        neighbors.push_back(GetPoint(GetCol(),GetRow()-1));

    if(CalcPos(GetCol(),GetRow()+1) >= 0)

        neighbors.push_back(GetPoint(GetCol(),GetRow()+1));

}

```



```

        return neighbors;
    }

OimDoc.h

CDataset* FirstDataset(void);

CDataset* NextDataset(void);

CDataset* CurrentDataset(void);

CDatapoint FirstPoint(void);

CDatapoint NextPoint(void);

VECTORDATAPOINT GetNeighbors(void);

void SetPoint(CDatapoint dp);

void SetIQ(float iq);

Protected variables

int m_CurrentDatasetIndex;

CDataset *m_pCurrentDataset;

OimDoc.cpp

CDataset* COimDoc::FirstDataset(void)

{

    m_CurrentDatasetIndex = 0;

```

```

        m_pCurrentDataset = GetDataset(m_CurrentDatasetIndex);

        return m_pCurrentDataset;
    }

    CDataset* COimDoc::NextDataset(void)
    {
        m_CurrentDatasetIndex++;

        m_pCurrentDataset = GetDataset(m_CurrentDatasetIndex);

        return m_pCurrentDataset;
    }

    CDataset* COimDoc::CurrentDataset(void)
    {
        return m_pCurrentDataset;
    }

    CDatapoint COimDoc::FirstPoint(void)
    {
        if(FirstDataset() != NULL)

            return m_pCurrentDataset->FirstPoint();

        else

            return CDatapoint();
    }

```

```

}

CDatapoint COimDoc::NextPoint(void)

{

    if(m_pCurrentDataset != NULL)

    {

        if(m_pCurrentDataset->NextPos() != -1)

        {

            return m_pCurrentDataset->CurrentPoint();

        }

        else

        {

            if(NextDataset() != NULL)

            {

                return m_pCurrentDataset->FirstPoint();

            }

            else

            {

                return CDatapoint();

            }

        }

    }

}

```

```

    }
}
else
{
    return CDatapoint();
}
}

VECTORDATAPOINT COimDoc::GetNeighbors(void)
{
    VECTORDATAPOINT neighbors;

    if(m_pCurrentDataset != NULL && m_pCurrentDataset->CurrentPos != -1)
    {
        // Points from up, down, left, right

        neighbors = m_pCurrentDataset->GetNeighbors();

        // Point from above

        CDataset *pPrevDataset = GetDataset(m_CurrentDatasetIndex-1);

        if(pPrevDataset != NULL)
        {

```

```

        CDatapoint dp =
pPrevDataset->GetPoint(m_pCurrentDataset->GetCol(),m_pCurrentDataset->GetRow());

        if(dp != CDatapoint())
        {
            neighbors.push_back(dp);
        }
    }

    // Point from below
    CDataset *pNextDataset = GetDataset(m_CurrentDatasetIndex+1);

    if(pNextDataset != NULL)
    {
        CDatapoint dp =
pNextDataset->GetPoint(m_pCurrentDataset->GetCol(),m_pCurrentDataset->GetRow());

        if(dp != CDatapoint())
        {
            neighbors.push_back(dp);
        }
    }
}

```

```

        return neighbors;
    }

void COimDoc::SetPoint(CDatapoint dp)
{
    if(m_pCurrentDataset != NULL)
    {
        m_pCurrentDataset->SetPoint(dp);
    }
}

```

```

void COimDoc::SetIQ(float iq)
{
    if(m_pCurrentDataset != NULL)
    {
        m_pCurrentDataset->SetIQ(iq);
    }
}

```

Mainfrm.cpp

```

VECTORDATAPOINT CDataset::GetNeighbors(void)
{
    VECTORDATAPOINT neighbors;

```

```

// Get points to the left and right of the current point
if(CalcPos(GetCol()-1,GetRow()) >= 0)
    neighbors.push_back(GetPoint(GetCol()-1,GetRow()));
else
    neighbors.push_back(CDatapoint());
if(CalcPos(GetCol()+1,GetRow()) >= 0)
    neighbors.push_back(GetPoint(GetCol()+1,GetRow()));
else
    neighbors.push_back(CDatapoint());
// Get points up and down from the current point
if(GetGridType() == GRID_HEX)
{
    if(CalcPos(GetCol(),GetRow()-2) >= 0)
        neighbors.push_back(GetPoint(GetCol(),GetRow()-2));
    else
        neighbors.push_back(CDatapoint());
    if(CalcPos(GetCol(),GetRow()+2) >= 0)
        neighbors.push_back(GetPoint(GetCol(),GetRow()+2));
    else
        neighbors.push_back(CDatapoint());
}
else
{

```

```

        if(CalcPos(GetCol(),GetRow()-1) >= 0)
            neighbors.push_back(GetPoint(GetCol(),GetRow()-1));
        else
            neighbors.push_back(CDatapoint());
        if(CalcPos(GetCol(),GetRow()+1) >= 0)
            neighbors.push_back(GetPoint(GetCol(),GetRow()+1));
        else
            neighbors.push_back(CDatapoint());
    }
    return neighbors;
}

VECTORDATAPOINT COimDoc::GetNeighbors(void)
{
    VECTORDATAPOINT neighbors;

    if(m_pCurrentDataset != NULL && m_pCurrentDataset->CurrentPos != -1)
    {
        // Points from up, down, left, right
        neighbors = m_pCurrentDataset->GetNeighbors();

        // Point from above
        CDataset *pPrevDataset = GetDataset(m_CurrentDatasetIndex-1);
        if(pPrevDataset != NULL)
        {
            CDatapoint dp = pPrevDataset->GetPoint(m_pCurrentDataset-

```



```

>GetCol(),m_pCurrentDataset->GetRow());
        neighbors.push_back(dp);
    }

    // Point from below
    CDataset *pNextDataset = GetDataset(m_CurrentDatasetIndex+1);
    if(pNextDataset != NULL)
    {
        CDatapoint dp = pNextDataset->GetPoint(m_pCurrentDataset-
>GetCol(),m_pCurrentDataset->GetRow());
        neighbors.push_back(dp);
    }
}

return neighbors;
}void CMainFrame::OnWizard()

{

/* The function is called from a button click. The code is executed from the
CMainFrame::OnWizard    *

* function is executed when you hit the Report Generator Template button in the toolbar. Later
add a    *

* new button to the toolbar and create a new function to handle it.    *

* This code will iterate through all of the points in all of the datasets in the project    *

```

```

* dp is the current point *
* The neighbors key *
* neighbor[0] = left *
* neighbor[1] = right *
* neighbor[2] = up *
* neighbor[3] = down *
* neighbor[4] = above (i.e. same point in previous dataset in project) *
* neighbor[5] = below (i.e. same point in next dataset in project) *
* Note that if the current point is on an edge then one of these neighbors will be invalid. *
* (i.e. be an empty Datapoint). You'll have to decide what to do in the case you are on an edge.*/

```

```
float va[18][9];
```

```
//Components of dyadic product of Burger's Vector and Line Direction of dislocations
used for minimization.
```

```

va[0][0] = -0.0044; va[0][1] = 0.144; va[0][2] = -0.2674; va[0][3] = -0.144; va[0][4] = -0.1741;
va[0][5] = 0.2674; va[0][6] = 0.0206; va[0][7] = -0.0206; va[0][8] = 0.0179; va[1][0] = -0.1433;
va[1][1] = 0.2561; va[1][2] = -0.1222; va[1][3] = -0.0087; va[1][4] = 0.01; va[1][5] = -0.0015;
va[1][6] = 0.1426; va[1][7] = -0.2664; va[1][8] = 0.1865; va[2][0] = 0.0487; va[2][1] = 0.0247;
va[2][2] = -0.0282; va[2][3] = -0.2721; va[2][4] = 0.1831; va[2][5] = 0.1519; va[2][6] = 0.2687;
va[2][7] = -0.1449; va[2][8] = -0.1964; va[3][0] = 0.203; va[3][1] = -0.1274; va[3][2] = 0.2367;
va[3][3] = 0.1274; va[3][4] = -0.2139; va[3][5] = 0.2995; va[3][6] = -0.0182; va[3][7] = -0.0231;

```

va[3][8] = 0.0011; va[4][0] = -0.2752; va[4][1] = -0.291; va[4][2] = 0.1869; va[4][3] = 0.0436;  
va[4][4] = 0.0353; va[4][5] = -0.0219; va[4][6] = -0.1476; va[4][7] = -0.2648; va[4][8] = 0.1972;  
va[5][0] = -0.0267; va[5][1] = -0.0229; va[5][2] = 0.0248; va[5][3] = 0.2703; va[5][4] = 0.1976;  
va[5][5] = 0.1402; va[5][6] = -0.2684; va[5][7] = -0.144; va[5][8] = -0.1903; va[6][0] = 0.203;  
va[6][1] = -0.1274; va[6][2] = -0.2995; va[6][3] = 0.1274; va[6][4] = -0.2139; va[6][5] = -  
0.2367;  
va[6][6] = 0.0231; va[6][7] = 0.0182; va[6][8] = 0.0011; va[7][0] = -0.2187; va[7][1] = -0.2863;  
va[7][2] = -0.1105; va[7][3] = 0.0389; va[7][4] = 0.0245; va[7][5] = -0.0545; va[7][6] = 0.1417;  
va[7][7] = 0.2707; va[7][8] = 0.1926; va[8][0] = -0.0833; va[8][1] = -0.0276; va[8][2] = -0.0778;  
va[8][3] = 0.275; va[8][4] = -0.2085; va[8][5] = -0.1572; va[8][6] = 0.2671; va[8][7] = 0.1453;  
va[8][8] = -0.1857; va[9][0] = 0.1464; va[9][1] = 0.1565; va[9][2] = 0.2454; va[9][3] = -0.1565;  
va[9][4] = -0.2031; va[9][5] = -0.2454; va[9][6] = -0.0189; va[9][7] = 0.0189; va[9][8] = 0.0057;  
va[10][0] = -0.2187; va[10][1] = 0.2499; va[10][2] = 0.1782; va[10][3] = -0.0024; va[10][4] =  
0.0245;  
va[10][5] = -0.0545; va[10][6] = -0.1469; va[10][7] = 0.2707; va[10][8] = 0.1926; va[11][0] = -  
0.0267;  
va[11][1] = 0.0184; va[11][2] = 0.0248; va[11][3] = -0.2659; va[11][4] = 0.1976; va[11][5] = -  
0.1485;  
va[11][6] = -0.2684; va[11][7] = 0.1447; va[11][8] = -0.1903; va[12][0] = 0.2771; va[12][1] =  
0.2374;

va[12][2] = -0.0429; va[12][3] = 0.1912; va[12][4] = 0.2499; va[12][5] = 0.0429; va[12][6] = 0.0033;

va[12][7] = -0.0033; va[12][8] = -0.0528; va[13][0] = 0.2662; va[13][1] = 0.0222; va[13][2] = 0.1731;

va[13][3] = -0.0222; va[13][4] = -0.0815; va[13][5] = 0.0412; va[13][6] = 0.2175; va[13][7] = -0.0032;

va[13][8] = 0.2816; va[14][0] = -0.0446; va[14][1] = -0.0037; va[14][2] = 0.0069; va[14][3] = 0.0037;

va[14][4] = 0.2813; va[14][5] = 0.2074; va[14][6] = -0.0005; va[14][7] = 0.2148; va[14][8] = 0.2764;

va[15][0] = 0.2771; va[15][1] = -0.1912; va[15][2] = -0.0429; va[15][3] = -0.2374; va[15][4] = 0.2499;

va[15][5] = 0.0429; va[15][6] = 0.0033; va[15][7] = -0.0033; va[15][8] = -0.0528; va[16][0] = 0.3642;

va[16][1] = 0.0303; va[16][2] = -0.2707; va[16][3] = -0.0303; va[16][4] = -0.1003; va[16][5] = 0.0564;

va[16][6] = -0.21; va[16][7] = -0.0043; va[16][8] = 0.2736; va[17][0] = -0.1426; va[17][1] = -0.0119;

va[17][2] = 0.0221; va[17][3] = 0.0119; va[17][4] = 0.3001; va[17][5] = -0.2364; va[17][6] = -0.0017;

va[17][7] = -0.2126; va[17][8] = 0.2843;

```

float xStep = GetOimDoc()->FirstDataset()->GetXStep();

float yStep = GetOimDoc()->FirstDataset()->GetYStep();

// Loop through all points

for(CDatapoint dp = GetOimDoc()->FirstPoint(); dp != CDatapoint(); dp =
GetOimDoc()->NextPoint())

{

VECTORDATAPOINT neighbors = GetOimDoc()->GetNeighbors();

// Get all of the neighbors of this point, above, below, up, down, left, right

float tot_GND;

tot_GND=0.0f;

// filter misorientation greater than 5 degrees for point to right

float mang = minAngSlns(GetOimDoc()->CurrentDataset()->GetPhase(dp.phase),dp.g,
neighbors[1].g);

// filter misorientation greater than 5 degrees for the point down

float mang1 = minAngSlns(GetOimDoc()->CurrentDataset()->GetPhase(dp.phase),dp.g,
neighbors[3].g);

// filter misorientation greater than 5 degrees for the point left

float mang2 = minAngSlns(GetOimDoc()->CurrentDataset()->GetPhase(dp.phase),dp.g,
neighbors[0].g);

```

```

// filter misorientation greater than 5 degrees for the point up

float mang3 = minAngSlns(GetOimDoc()->CurrentDataset()->GetPhase(dp.phase),dp.g,
neighbors[2].g);

// filter misorientation greater than 5 degrees for the point above

float mang4 = minAngSlns(GetOimDoc()->CurrentDataset()->GetPhase(dp.phase),dp.g,
neighbors[4].g);

// filter misorientation greater than 5 degrees for the point below

float mang5 = minAngSlns(GetOimDoc()->CurrentDataset()->GetPhase(dp.phase),dp.g,
neighbors[5].g);

// check to see if we are on the edge

bool OnEdgePoint = false;

for(int i=0; i<neighbors.size(); i++)

{

    if(neighbors[i] == CDatapoint())

        {

            OnEdgePoint = true;

            break;

        }

}

if(mang < 5.000 && mang1 < 5.000 && !OnEdgePoint)

```

```

{
    CRodrigues rod;

    rodrigues r;

    float gPoint[3][3], gLeft[3][3], gRight[3][3], gUp[3][3], gDown[3][3], gAbove[3][3],
gBelow[3][3];

        int k,l;

    // Current point
    rod.reduction_to_SEA(dp.g,r);

    RodVTogMat(r.rod[0], r.rod[1], r.rod[2], gPoint);

    // Left neighbor
    if(neighbors[0] != CDatapoint())
    {
        rod.reduction_to_SEA(neighbors[0].g, r);

        RodVTogMat(r.rod[0], r.rod[1], r.rod[2], gLeft);
    }
    else
        {
            for (k=0; k<3; ++k) for (l=0; l<3; ++l)
                {
                    gLeft[k][l] = 0.0f;

```

```

        }
    }

    // Right neighbor
if(neighbors[1] != CDatapoint())
{
    rod.reduction_to_SEA(neighbors[1].g, r);

    RodVTogMat(r.rod[0], r.rod[1], r.rod[2], gRight);
}

    else
    {
        for (k=0; k<3; ++k) for (l=0; l<3; ++l)
        {
            gRight[k][l] = 0.0f;
        }
    }

// Up neighbor
if(neighbors[2] != CDatapoint())
{
    rod.reduction_to_SEA(neighbors[2].g, r);
}

```



```

RodVTogMat(r.rod[0], r.rod[1], r.rod[2], gUp);
}

else

{

for (k=0; k<3; ++k) for (l=0; l<3; ++l)

{

gUp[k][l] = 0.0f;

}

}

// Down neighbor

if(neighbors[3] != CDatapoint())

{

rod.reduction_to_SEA(neighbors[3].g, r);

RodVTogMat(r.rod[0], r.rod[1], r.rod[2], gDown);

}

else

{

for (k=0; k<3; ++k) for (l=0; l<3; ++l)

{

```

```

                                gDown[k][l] = 0.0f;
                                }
                            }

// Above neighbor

if(neighbors[4] != CDatapoint())
{
    rod.reduction_to_SEA(neighbors[4].g, r);

    RodVTogMat(r.rod[0], r.rod[1], r.rod[2], gAbove);
}

    else
    {
        for (k=0; k<3; ++k) for (l=0; l<3; ++l)
        {
            gAbove[k][l] = 0.0f;
        }
    }

// Below neighbor

if(neighbors[5] != CDatapoint())
{

```

```

rod.reduction_to_SEA(neighbors[5].g, r);

RodVTogMat(r.rod[0], r.rod[1], r.rod[2], gBelow);

}

else

{

    for (k=0; k<3; ++k) for (l=0; l<3; ++l)

    {

        gBelow[k][l] = 0.0f;

    }

}

// Secondary minimum angle filter that excludes data that falls out side the vector domain.

if (fabs(gPoint[0][0] - gRight[0][0]) < 0.05 && fabs(gPoint[1][2] - gRight[1][2]) < 0.05 &&
fabs(gPoint[1][0] - gRight[1][0]) < 0.05 && fabs(gPoint[0][0] - gDown[0][0]) < 0.05 &&
fabs(gPoint[1][2] - gDown[1][2]) < 0.05 && fabs(gPoint[1][0] - gDown[1][0]) < 0.05)

{

//if ((fabs(gPoint[0][0] - gRight[0][2]) < 0.1 && fabs(gPoint[1][2] - gRight[1][2]) < 0.1 &&
fabs(gPoint[2][2] - gRight[2][2]) < 0.1) &&

```

```

// (fabs(gPoint[0][0] - gLeft[0][2]) < 0.1 && fabs(gPoint[1][2] - gLeft[1][2]) < 0.1 &&
fabs(gPoint[2][2] - gLeft[2][2]) < 0.1) &&

// fabs(gPoint[0][2] - gDown[0][2]) < 0.1 && fabs(gPoint[1][2] - gDown[1][2]) < 0.1 &&
fabs(gPoint[2][2] - gDown[2][2]) < 0.1) &&

// fabs(gPoint[0][0] - gUp[0][2]) < 0.1 && fabs(gPoint[1][2] - gUp[1][2]) < 0.1 &&
fabs(gPoint[2][2] - gUp[2][2]) < 0.1) &&

// (fabs(gPoint[0][1] - gAbove[0][1]) < 0.1 && fabs(gPoint[1][1] - gAbove[1][1]) < 0.1 &&
fabs(gPoint[2][1] - gAbove[2][1]) < 0.1) &&

// (fabs(gPoint[0][1] - gBelow[0][1]) < 0.1 && fabs(gPoint[1][1] - gBelow[1][1]) < 0.1 &&
fabs(gPoint[2][1] - gBelow[2][1]) < 0.1)

// {

// Calculates Dislocation Density Tensor

float alpha[9];

alpha[0] = 0.5f*(((gDown[0][2]-gPoint[0][2])/(2.0f*yStep))-((gBelow[0][1]-
gPoint[0][1])/(m_zSlice)))+0.5f*(((gUp[0][2]-gPoint[0][2])/(2.0f*yStep))-((gAbove[0][1]-
gPoint[0][1])/m_zSlice));

alpha[1] = 0.5f*(((gDown[1][2]-gPoint[1][2])/(2.0f*yStep))-((gBelow[1][1]-
gPoint[1][1])/(m_zSlice)))+0.5f*(((gUp[1][2]-gPoint[1][2])/(2.0f*yStep))-((gAbove[1][1]-
gPoint[1][1])/m_zSlice));

```

$$\alpha[2] = 0.5f*(((gDown[2][2]-gPoint[2][2])/(2.0f*yStep))-((gBelow[2][1]-gPoint[2][1])/(m\_zSlice)))+0.5f*(((gUp[2][2]-gPoint[2][2])/(2.0f*yStep))-((gAbove[2][1]-gPoint[2][1])/(m\_zSlice)));$$

$$\alpha[3] = 0.5f*(((gBelow[0][0]-gPoint[0][0])/m\_zSlice)-((gRight[0][2]-gPoint[0][2])/xStep))+0.5f*(((gAbove[0][0]-gPoint[0][0])/m\_zSlice)-((gLeft[0][2]-gPoint[0][2])/xStep));$$

$$\alpha[4] = 0.5f*(((gBelow[1][0]-gPoint[1][0])/m\_zSlice)-((gRight[1][2]-gPoint[1][2])/xStep))+0.5f*(((gAbove[1][0]-gPoint[1][0])/m\_zSlice)-((gLeft[1][2]-gPoint[1][2])/xStep));$$

$$\alpha[5] = 0.5f*(((gBelow[2][0]-gPoint[2][0])/m\_zSlice)-((gRight[2][2]-gPoint[2][2])/xStep))+0.5f*(((gAbove[2][0]-gPoint[2][0])/m\_zSlice)-((gLeft[2][2]-gPoint[2][2])/xStep));$$

$$\alpha[6] = 0.5f*(((gRight[0][1]-gPoint[0][1])/xStep)-((gDown[0][0]-gPoint[0][0])/(2.0f*yStep)))+0.5f*(((gLeft[0][1]-gPoint[0][1])/xStep)-((gUp[0][0]-gPoint[0][0])/(2.0f*yStep)));$$

$$\alpha[7] = 0.5f*(((gRight[1][1]-gPoint[1][1])/xStep)-((gDown[1][0]-gPoint[1][0])/(2.0f*yStep)))+0.5f*(((gLeft[1][1]-gPoint[1][1])/xStep)-((gUp[1][0]-gPoint[1][0])/(2.0f*yStep)));$$

$$\alpha[8] = 0.5f*(((gRight[2][1]-gPoint[2][1])/xStep)-((gDown[2][0]-gPoint[2][0])/(2.0f*yStep)))+0.5f*(((gLeft[2][1]-gPoint[2][1])/m\_zSlice)-((gUp[2][0]-gPoint[2][0])/(2.0f*yStep)));$$

```

        int i,j;

        for (i=0; i<18; ++i) for (j=0; j<9; ++j)

        {

                float val = va[i][j]*alpha[j];

                tot_GND+= fabs(val);

        }

    }

}

int total = (((tot_GND/0.000286)) + 0.5);

// replace ci with tot_GND in the datapoint at p for Aluminum

GetOimDoc()->SetIQ(total);    // Set the iq of the current point

// replace ci with tot_GND in the datapoint at p for Copper

//GetOimDoc()->SetIQ((int)(((tot_GND/0.000256)) + 0.5));

}

for (CDataSet* pDataset = GetOimDoc()->FirstDataset(); pDataset != NULL; pDataset =
GetOimDoc()->NextDataset())

pDataset->CalcValues();

GetOimDoc()->Update(FORCE_UPDATE, 0);

}

```